

Entropy conservative and entropy stable solid wall boundary conditions for the resistive magnetohydrodynamic equations

Vladimir Pimanov^a, Lisandro Dalcin^a, Matteo Parsani^{a,b,*}

^a*King Abdullah University of Science and Technology (KAUST), Computer Electrical and Mathematical Science and Engineering Division (CEMSE), Extreme Computing Research Center (ECRC), Thuwal, Saudi Arabia*

^b*King Abdullah University of Science and Technology (KAUST), Physical Science and Engineering Division (PSE), Thuwal, Saudi Arabia*

Abstract

We present a novel technique for imposing non-linear entropy conservative and entropy stable wall boundary conditions for the resistive magnetohydrodynamic equations in the presence of an adiabatic wall or a wall with a prescribed heat entropy flow, addressing three scenarios: electrically insulating walls, thin walls with finite conductivity, and perfectly conducting walls. The procedure relies on the formalism and mimetic properties of diagonal-norm, summation-by-parts, and simultaneous-approximation-term operators. Using the method of lines, a semi-discrete entropy estimate for the entire domain is obtained when the proposed numerical imposition of boundary conditions is coupled with an entropy-conservative or entropy-stable discrete interior operator. The resulting estimate mimics the global entropy estimate obtained at the continuous level. The boundary data at the wall are weakly imposed using a penalty flux approach and a simultaneous-approximation-term technique for both the conservative variables and the gradient of the entropy variables. Discontinuous spectral collocation operators (mass lumped nodal discontinuous Galerkin operators) on high-order unstructured grids are used to demonstrate the new procedure's accuracy, robustness, and efficacy for weakly enforcing boundary conditions. Numerical simulations confirm the non-linear stability of the proposed technique, with applications to three-dimensional flows. The procedure described is compatible with any diagonal-norm summation-by-parts spatial operator, including finite element, finite difference, finite volume, nodal and modal discontinuous Galerkin, and flux reconstruction schemes.

Keywords: Magnetohydrodynamic equations, Electrically conducting walls, Electrically insulating walls, Entropy conservation, Entropy stability, Summation-by-parts operators, Simultaneous-approximation-terms

1. Introduction

The resistive magnetohydrodynamics (MHD) equations [1–4] govern the motion of ionized plasma and electrically conducting fluids and are of great interest in space physics, astrophysics,

*Corresponding author.

Email addresses: vladimir.pimanov@kaust.edu.sa (Vladimir Pimanov), dalcinl@gmail.com (Lisandro Dalcin), matteo.parsani@kaust.edu.sa (Matteo Parsani)

and many other technical applications. One of these critical applications is nuclear fusion energy generation [5, 6].

The resistive MHD equations for compressible flows explicitly establish the conservation of mass, momentum, total energy, and magnetic fields. These equations also encapsulate two implicit principles. The first principle demands a divergence-free constraint on the magnetic field. At the continuum level, a divergence-free initial state guarantees the fulfillment of this principle at any subsequent time. However, numerical schemes often struggle to maintain this property due to accumulating numerical errors. Thus, special attention is required to fulfill this principle at the semi-discrete and fully-discrete levels. The second fundamental property of the resistive MHD equations is they satisfy the second law of thermodynamics. The total thermodynamic entropy can not decrease in time if the physical system is closed. Its variation is associated with two mechanisms: the production of entropy on discontinuities of the solution and diffusion mechanisms. The MHD equations meet this second principle because they are equipped with an additional non-conservative term proportional to the magnetic field divergence [1]. This non-conservative term is known as the Powell term [7]. Also, in this case, numerical schemes often struggle to maintain this property due to accumulating numerical errors.

Having the second law of thermodynamics built-in plays a unique role. Very often, this thermodynamic principle is at the core of the construction of semi-discrete and fully-discrete algorithms that are non-linearly stable (depending on the field, this property is also called entropy stability or Lyapunov stability) – provided that the positivity of the solution is preserved. In particular, in closed systems, under the physically informed assumptions of density and pressure positivity, the fulfillment of the second law of thermodynamic establishes an upper bound on the L_2 norm of the conservative variables (see, for instance, [8]) which can be translated into an upper bound of the primitive variables. Mimicking the continuous analyses at the discrete level is a rigorous way to develop robust, non-linearly stable numerical discretizations.

At the semi-discrete level, this work focuses on collocated discontinuous Galerkin (DG) discretizations for unstructured grids. For a high-order accurate representation of the solution, these methods deliver a high computation-to-communication ratio, which makes them a natural choice for the current and future generation of heterogeneous data-centric computing hardware [9–11]. In particular, they deliver better accuracy per degree of freedom than low-order counterparts, which leads to much smaller numerical errors in terms of dispersion and dissipation [12–14]. However, high-order accurate schemes generally suffer from instabilities more often than low-order schemes due to discontinuities in the solution or under-resolved physical features.

In the last two decades, entropy stable discontinuous Galerkin methods have been developed to solve several systems of hyperbolic equations, including the compressible Euler equations and the compressible Navier–Stokes equations; see, for instance, [15, 16]. An entropy stable discontinuous Galerkin spectral element method (DGSEM) for the resistive MHD equations is presented for spatially periodic solutions in domains without boundaries in [17]. In [18], the solver above is coupled with a classical finite volume discretization for shockwave capturing. To deal with divergence-free constrain on the magnetic field, the numerical schemes in [17, 18] are designed using a generalized Lagrange multiplier, providing divergence-cleaning properties to the spatial discretizations [19].

Issues remain on the path toward complete entropy stability for the MHD equations, *e.g.*, bound-preserving limiter for high-order accurate discretizations. In particular, one major obstacle is the need for boundary conditions that preserve the entropy conservation or stability property of the interior operators. Practical experience indicates that numerical instabilities frequently

originate at domain boundaries, where “the action takes place”. For instance, the interaction of shocks with these physical boundaries is particularly challenging for high-order formulations. In this article, we expand upon the method presented in [17] to introduce entropy conservative and entropy stable solid wall boundary conditions. The starting points are the entropy stable solid wall boundary conditions developed for the compressible Navier–Stokes equations in [20, 21] for collocated discontinuous Galerkin methods with the summation-by-parts property (DG-SBP) and simultaneous-approximation-terms (SATs) operators [16, 22, 23]. To develop the new boundary conditions, we consider a general conducting wall with conductance parameter c and address three scenarios: electrically insulating walls ($c = 0$), thin walls with finite conductivity ($0 < c < \infty$), and perfectly conducting walls ($c = \infty$).

We demonstrate the accuracy of the proposed boundary conditions through a convergence study towards an analytical solution in a circular pipe under a varying wall conductance parameter. The choice of pipe flow as a case study is strategic, showcasing the method’s efficacy in curved geometries, where meshes with curved elements are often used in conjunction with high-order accurate schemes. To verify the entropy conservative properties of the spatial discretization algorithm and our proposed hydrodynamic, thermal, and magnetic boundary conditions, we study the time rate of change of the entropy function of a flow around a stationary rotating spheroid. Finally, we test the new boundary conditions in two applications: fluid flow in a microchannel and a self-field magnetoplasmadynamic thruster.

The manuscript is organized as follows. Section 2 introduces the continuous formulation of the problem, including the notation and the system of governing equations, boundary conditions, and a thermodynamic analysis of the system. Section 3 details the one-dimensional DG-SBP-SAT discretization of the system and dives into the development of the new entropy-stable solid-wall boundary conditions. Section 5 discusses the numerical results that support the primary goal of this study. The concluding remarks are presented in Section 6.

2. Resistive compressible MHD equations

The compressible resistive magnetohydrodynamics (MHD) equations [1] and the formulation of an entropy stable discontinuous Galerkin method with the summation-by-part property (DG-SBP) are described in detail in [17]. Here, we summarize the continuous equations and their key properties, keeping the notation close to that of [17]. We also extend the continuous analysis to include entropy conservative and entropy stable solid wall boundary conditions.

2.1. Notation

We assume to work in a three-dimensional space, *i.e.*, in \mathbb{R}^3 . Spatial vectors are denoted with an arrow (*e.g.*, $\vec{v} = (v_1, v_2, v_3) \in \mathbb{R}^{1 \times 3}$). State vectors are denoted in bold (*e.g.*, $\mathbf{u} = (\rho, \rho\vec{v}, E, \vec{B}, \psi)^T \in \mathbb{R}^{9 \times 1}$). Block vectors are vectors that contain state vectors in each spatial direction, they are denoted in bold with double arrow (*e.g.*, $\overleftrightarrow{\mathbf{f}} = (\mathbf{f}_1, \mathbf{f}_2, \mathbf{f}_3) \in \mathbb{R}^{9 \times 3}$).

In Cartesian coordinates (x_1, x_2, x_3) , the gradient of a state vector is a block vector,

$$\overleftrightarrow{\nabla} \mathbf{u} = (\partial_{x_1} \mathbf{u}, \partial_{x_2} \mathbf{u}, \partial_{x_3} \mathbf{u}). \quad (2.1)$$

The gradient of a spatial vector is a second order tensor and in matrix form is given by

$$\overleftrightarrow{\nabla} \vec{v} = \begin{pmatrix} \partial_{x_1} v_1 & \partial_{x_2} v_1 & \partial_{x_3} v_1 \\ \partial_{x_1} v_2 & \partial_{x_2} v_2 & \partial_{x_3} v_2 \\ \partial_{x_1} v_3 & \partial_{x_2} v_3 & \partial_{x_3} v_3 \end{pmatrix}. \quad (2.2)$$

The divergence of a block vector is defined as

$$\vec{\nabla} \cdot \vec{\mathbf{f}} \stackrel{\leftrightarrow}{=} \partial_{x_1} \mathbf{f}_1 + \partial_{x_2} \mathbf{f}_2 + \partial_{x_3} \mathbf{f}_3. \quad (2.3)$$

We additionally define the jump operator, arithmetic, and logarithmic means between two values a_L and a_R as

$$\llbracket a \rrbracket_{(L,R)} := a_R - a_L, \quad \{\{a\}\}_{(L,R)} := \frac{1}{2}(a_R + a_L), \quad a_{(L,R)}^{\ln} := \llbracket a \rrbracket_{(L,R)} / \llbracket \ln(a) \rrbracket_{(L,R)}. \quad (2.4)$$

A numerically stable procedure to evaluate the logarithmic mean is given in [24].

2.2. The system of PDEs

We consider the compressible visco-resistive MHD equations compatible with the continuous entropy analysis presented by Godunov in 1972 [1]. This system of PDEs reads

$$\begin{aligned} \partial_t \mathbf{u} + \vec{\nabla} \cdot \vec{\mathbf{f}}^a(\mathbf{u}) + \Upsilon(\mathbf{u}, \vec{\nabla} \mathbf{u}) &= \vec{\nabla} \cdot \vec{\mathbf{f}}^\nu(\mathbf{u}, \vec{\nabla} \mathbf{u}) + \mathbf{r}(\mathbf{u}), \quad \forall \vec{x} \in \Omega, \quad t > 0, \\ \Pi(\mathbf{u}, \vec{\nabla} \mathbf{u}) &= 0, \quad \forall \vec{x} \in \Gamma, \quad t > 0, \\ \mathbf{u} &= \mathbf{u}^{\text{init}}, \quad \forall \vec{x} \in \Omega, \quad t = 0, \end{aligned} \quad (2.5)$$

where \mathbf{u} is the state vector, $\vec{\mathbf{f}}^a$ and $\vec{\mathbf{f}}^\nu$ are advective and diffusive fluxes, and Υ is the non-conservative term which enhances the numerical properties of system (2.5) and ensures it is symmetrizable, extending the original ideas from [1, 7] to the ideal GLM-MHD system reported in [19]. The vector \mathbf{r} is a purely algebraic source term introduced to dampen the magnetic field's divergence-free numerical error. The Greek letter Ω indicates the spatial domain with boundary Γ . Boundary conditions are expressed in a general form through an implicit function Π . In the generalized Lagrangian multiplier (GLM) formulation of the MHD equations (GLM-MHD), the state vector is given by $\mathbf{u} = (\rho, \rho \vec{v}, E, \vec{B}, \psi)^T$, where ρ is the density, $\vec{v} = (v_1, v_2, v_3)$ is the velocity, E is the total energy, $\vec{B} = (B_1, B_2, B_3)$ is the magnetic field, ψ is the generalized Lagrange multiplier introduced in [19] for the purpose of magnetic field divergence cleaning. The introduction of the generalized Lagrange multiplier builds on the original ideas from [25, 26]. Note that if the viscous fluxes are set to zero, the ideal MHD for compressible flows are recovered. In this work, we consider the perfect gas model.

The advective flux, split into the Euler (*i.e.*, the inviscid part of the compressible Navier–Stokes equations), ideal MHD, and GLM parts, is

$$\vec{\mathbf{f}}^a(\mathbf{u}) = \begin{pmatrix} \rho \vec{v} \\ \rho \vec{v}^T \vec{v} + p \underline{I} \\ \left(\frac{1}{2} \rho \|\vec{v}\|^2 + \frac{\gamma p}{\gamma - 1} \right) \vec{v} \\ \underline{0} \\ \underline{0} \end{pmatrix} + \begin{pmatrix} \underline{0} \\ \frac{1}{2\mu_0} \|\vec{B}\|^2 \underline{I} - \frac{1}{\mu_0} \vec{B}^T \vec{B} \\ \frac{1}{\mu_0} \left(\|\vec{B}\|^2 \vec{v} - (\vec{v} \cdot \vec{B}) \vec{B} \right) \\ \vec{B}^T \vec{v} - \vec{v}^T \vec{B} \\ \underline{0} \end{pmatrix} + \begin{pmatrix} \underline{0} \\ \underline{0} \\ \frac{c_h}{\mu_0} \psi \vec{B} \\ c_h \psi \underline{I} \\ c_h \vec{B} \end{pmatrix}, \quad (2.6)$$

where p is the gas pressure, \underline{I} is the 3×3 identity matrix, μ_0 is the permeability of the medium, γ is the heat capacity ratio, and c_h is the hyperbolic divergence cleaning speed.

The non-conservative term, Υ , consists of two components, namely $\Upsilon = \Upsilon^{\text{MHD}} + \Upsilon^{\text{GLM}}$. The first non-conservative term, Υ^{MHD} , also known as the Powell term [7], reads

$$\Upsilon^{\text{MHD}} = (\vec{\nabla} \cdot \vec{B}) \phi^{\text{MHD}} = (\vec{\nabla} \cdot \vec{B}) \left(0, \frac{1}{\mu_0} \vec{B}, \frac{1}{\mu_0} \vec{v} \cdot \vec{B}, \vec{v}, 0 \right)^T. \quad (2.7)$$

The second non-conservative term, Υ^{GLM} , guarantees Galilean invariance of the GLM-MHD equations and is given by

$$\Upsilon^{\text{GLM}} = \overleftrightarrow{\phi}^{\text{GLM}} \cdot \vec{\nabla} \psi = \phi_1^{\text{GLM}} \partial_{x_1} \psi + \phi_2^{\text{GLM}} \partial_{x_2} \psi + \phi_3^{\text{GLM}} \partial_{x_3} \psi, \quad (2.8)$$

where $\phi_l^{\text{GLM}} = \left(0, \vec{0}, \mu_0^{-1} v_l \psi, \vec{0}, v_l \right)^T$.

At the continuous level, $\vec{\nabla} \cdot \vec{B} = 0$. Consequently, the non-conservative term, Υ^{MHD} , is also zero. For a more detailed discussion of the model and its derivation, we refer the reader to [19].

The diffusive flux includes electroresistive, viscous, and thermoconductive effects and reads

$$\overleftrightarrow{\mathbf{f}}^\nu(\mathbf{u}, \vec{\nabla} \mathbf{u}) = \begin{pmatrix} \vec{0} \\ \underline{\tau} \\ \vec{v} \underline{\tau} - \vec{q} - \frac{\mu_R}{\mu_0^2} (\vec{\nabla} \times \vec{B}) \times \vec{B} \\ \frac{\mu_R}{\mu_0} (\vec{\nabla} \vec{B} - (\vec{\nabla} \vec{B})^T) \\ \vec{0} \end{pmatrix}, \quad (2.9)$$

where $\underline{\tau}$ is the stress tensor,

$$\underline{\tau} = \mu_{NS} \left(\vec{\nabla} \vec{v} + (\vec{\nabla} \vec{v})^T \right) - \frac{2}{3} \mu_{NS} \left(\vec{\nabla} \cdot \vec{v} \right) \underline{I}, \quad (2.10)$$

and \vec{q} is the heat flux, linearly proportional to the gradient of temperature, T , via the Fourier's law, *i.e.*,

$$\vec{q} = -\kappa \vec{\nabla} T. \quad (2.11)$$

The physical parameters μ_{NS} , μ_R , and κ are the fluid dynamic viscosity, the resistivity of the plasma, and the thermal conductivity, respectively. The symbol R indicates the specific gas constant and is given by $R = R_u/M_w$, where R_u is the universal gas constant, and M_w is the molecular weight of the gas. Here, because we consider the perfect gas model, the equation for the temperature is given by $T = p/\rho R$ whereas, the pressure, extended to account for the GLM term, reads

$$p = (\gamma - 1) \left(E - \frac{1}{2} \rho \|\vec{v}\|^2 - \frac{1}{2\mu_0} \|\vec{B}\|^2 - \frac{1}{2\mu_0} \psi^2 \right). \quad (2.12)$$

If otherwise stated, the algebraic source term \mathbf{r} is given by

$$\mathbf{r} = \left(0, \vec{0}, 0, \vec{0}, -\alpha \psi \right)^T, \quad (2.13)$$

with $\alpha \geq 0$. We reiterate that introducing this algebraic source term enhances the cleaning of the $\vec{\nabla} \cdot \vec{B}$ at the semi-discrete level [26, 27] (*i.e.*, of the spatial discretization). Specifically, an additional damping on the numerical error of the divergence-free magnetic field is attained if $\alpha > 0$.

2.3. Thermodynamic properties of the system

As shown in [17, 19], the GLM-MHD system (2.5) adheres to the second law of thermodynamics. In fact, it possesses a strictly convex entropy function, $S(\mathbf{u})$,

$$S(\mathbf{u}) = -\rho s, \quad (2.14)$$

which is proportional (with the negative sign) to the specific thermodynamic entropy

$$s = \frac{R}{\gamma - 1} \ln \left(\frac{T}{T^*} \right) - R \ln \left(\frac{\rho}{\rho^*} \right), \quad (2.15)$$

where T^* and ρ^* are the reference values for temperature and pressure, respectively. The entropy function $S(\mathbf{u})$ is strictly convex on its arguments in a bounded domain Ω under the physically informed assumption that

$$T > 0, \quad \rho > 0, \quad \forall \vec{x} \in \Omega, \quad t \geq 0. \quad (2.16)$$

In this work, we assume (2.16) to be always true. The convexity of the entropy function is a valuable tool for providing stability for the PDE system in the L^2 norm [8, 28].

Differentiating the entropy function with respect to the conservative variables leads to the definition of the entropy variables \mathbf{w} ,

$$\mathbf{w}^T = \frac{\partial S}{\partial \mathbf{u}} = \left(\frac{\gamma R}{\gamma - 1} - s - \frac{1}{2} \frac{\|\vec{v}\|^2}{T}, \quad \frac{\vec{v}}{T}, \quad -\frac{1}{T}, \quad \frac{1}{\mu_0} \frac{\vec{B}}{T}, \quad \frac{1}{\mu_0} \frac{\psi}{T} \right). \quad (2.17)$$

The convexity of the entropy function guarantees the invertibility of the mapping between the entropy and the conservative variables.

If the solution is smooth, contracting the entropy variables with the conservation equations (2.5) yields the (scalar) conservation equation for the entropy function,

$$\frac{\partial S}{\partial t} + \vec{\nabla} \cdot \vec{f}^S = \mathbf{w}^T \left(\vec{\nabla} \cdot \overset{\leftrightarrow}{\mathbf{f}}^\nu \right) + \mathbf{w}^T \mathbf{r}, \quad (2.18)$$

where $\vec{f}^S = S \vec{v}$ is the entropy flux which, as shown in [19] for GLM-MHD system, satisfies the identity

$$\vec{\nabla} \cdot \vec{f}^S = \mathbf{w}^T \vec{\nabla} \cdot \overset{\leftrightarrow}{\mathbf{f}}^a + \mathbf{w}^T \Upsilon. \quad (2.19)$$

In entropy variables, the diffusive flux $\overset{\leftrightarrow}{\mathbf{f}}^\nu = (\mathbf{f}_1^\nu, \mathbf{f}_2^\nu, \mathbf{f}_3^\nu)$ takes the following (matrix-vector multiplication) form:

$$\mathbf{f}_i^\nu = \sum_{j=1}^3 C_{ij}^\nu \frac{\partial \mathbf{w}}{\partial x_j}. \quad (2.20)$$

The 3×3 block matrix, compiled from 9 matrices C_{ij}^ν of size 9×9 each, appearing in (2.20), is symmetric positive semi-definite. With the definition (2.13) and the positivity assumption (2.16), the last term in (2.18) equals

$$\mathbf{w}^T \mathbf{r} = -\frac{\alpha \psi^2}{\mu_0 T} \quad (2.21)$$

and is non-positive.

Considering (2.20) and (2.21), integrating (2.18) over the domain Ω with boundary Γ , and invoking the divergence theorem leads to the following scalar global equation for the entropy function:

$$\frac{d}{dt} \int_{\Omega} S d\Omega \leq \oint_{\Gamma} (\mathbf{w}^T \mathbf{f}_n^\nu - f_n^S) d\Gamma - \int_{\Omega} \left(\frac{\partial \mathbf{w}}{\partial x_i} \right)^T C_{ij}^\nu \left(\frac{\partial \mathbf{w}}{\partial x_j} \right) d\Omega - \int_{\Omega} \frac{\alpha \psi^2}{\mu_0 T} d\Omega, \quad (2.22)$$

where \mathbf{f}_n^ν and f_n^S are the normal components to the boundary of the corresponding vectors. For a smooth solution, (2.22) takes the form of an equality. The semi-positiveness of the matrices C_{ij}^ν and the non-negativeness of the coefficient α guarantee the volume integrals on the right-hand side of inequality (2.22) are non-positive. Therefore, the entropy in Ω can only increase through the flux across the boundary Γ , *i.e.*, the integral term on the right-hand side of (2.22). This is the same term appearing in the entropy stability analysis of the compressible Navier–Stokes. Therefore, the following two theorems presented in [20] and [21] bound the flux of entropy through a solid wall and, hence, the time derivative of the entropy function given in (2.22).

The first theorem is a generalization of Theorem 2.2 from [20] (see also Theorem 3.1 in [21]) from the compressible Navier–Stokes equations to the compressible GLM-MHD system (2.5).

Theorem 1. *At a solid wall, the condition*

$$\vec{v} = \vec{v}^w, \quad \vec{v}^w \cdot \vec{n} = 0, \quad \forall \vec{x} \in \Gamma, \quad t \geq 0, \quad (2.23)$$

where \vec{v}^w represents the wall velocity and \vec{n} is the unit outward normal vector to the wall, bounds the advective contribution to the time derivative of the entropy in equation (2.22).

PROOF. The normal advective entropy flux $f_n^S = Sv_n$ in equation (2.22) equals zero at the wall. \square

The next theorem is an extension of Theorem 3.2 from [21] from the compressible Navier–Stokes equations to the GLM-MHD system (2.5).

Theorem 2. *The wall boundary condition (or prescription of a heat entropy flux, also known as heat entropy transfer)*

$$g(t) = \kappa \frac{1}{T} \frac{\partial T}{\partial n}, \quad \forall \vec{x} \in \Gamma, \quad t \geq 0, \quad (2.24)$$

where $\partial T / \partial n$ denotes the temperature gradient normal to the wall, bounds the diffusive contribution to the time derivative of the entropy in (2.22).

PROOF. Contraction of the normal diffusive flux, \mathbf{f}_n^ν , with the entropy variables, \mathbf{w} , reads,

$$\begin{aligned} \mathbf{w}^T \mathbf{f}_n^\nu &= \frac{\vec{v} \cdot \vec{\tau}_n}{T} - \frac{1}{T} \left(\vec{v} \cdot \vec{\tau}_n - \kappa \frac{\partial T}{\partial n} - \frac{\mu_R}{\mu_0^2} \left((\vec{\nabla} \times \vec{B}) \times \vec{B} \right)_n \right) + \frac{\vec{B}}{\mu_0 T} \frac{\mu_R}{\mu_0} \left(\vec{\nabla} \vec{B} - (\vec{\nabla} \vec{B})^T \right)_n \\ &= \kappa \frac{\partial T}{\partial n} \frac{1}{T} = g(t), \end{aligned}$$

where the subscript n denotes normal component to the wall of the corresponding tensor. Therefore, the prescribed boundary entropy flux (or entropy transfer) function $g(t)$ bounds the diffusive contribution to the time derivative of the entropy in (2.22). \square

Remark 1. As outlined in [21], this boundary condition at first glance appears “uncommon”. However, the scalar value $\kappa \frac{1}{T} \frac{\partial T}{\partial n}$ accounts for the change in entropy at the boundary and matches the result of the thermodynamic (entropy) analysis of a generic system [29]. In fact, the compressible Navier–Stokes model encapsulates correctly the thermodynamic analysis at the boundary of the domain, Ω .

It is essential to understand that the boundary term $\kappa \frac{1}{T} \frac{\partial T}{\partial n}$ is not a peculiar term only for a wall [21]. It is the contribution of a generic piece of boundary of Γ to the entropy analysis. Thus, the development of any entropy conservative and entropy stable boundary conditions for the compressible Navier–Stokes equations and the GLM-MHD system (2.5) have to provide a proper treatment for it.

2.4. Solid wall boundary conditions

In the previous subsection, we have shown that when considering a solid wall, the entropy analysis of the GLM-MHD system (2.5) yields entropy conservative and entropy stable boundary conditions, which are the same as those obtained for the compressible Navier–Stokes equations [20, 21]. Thus, the entropy analysis of the GLM-MHD system (2.5) does not provide information on if and how boundary conditions must be specified for the magnetic field \vec{B} and the generalized Lagrange multiplier ψ . In this work, we develop new discrete entropy conservative and entropy stable solid wall boundary conditions for the magnetic field, which mimic the solid wall boundary conditions for the resistive MHD equations [2].

Magnetic wall boundary conditions come in different forms depending on the conductive properties of the wall. We refer the reader to the book of Davidson [2] for a detailed discussion and derivation of magnetic boundary conditions for electrically (perfectly) insulating walls, electrically conducting thin walls, and electrically perfectly conducting walls.

For electrically insulating walls, the magnetic field is prescribed at a boundary Γ^{ins} as

$$\vec{B} = \vec{B}^0, \quad \forall \vec{x} \in \Gamma^{\text{ins}}, \quad t \geq 0, \quad (2.25)$$

where \vec{B}^0 is the external magnetic field. This condition follows from the assumption that no electric current flows from the fluid to the wall or within the wall. Consequently, there is no jump in the magnetic field across the fluid-solid interface. Since no electric current flows through the wall, an additional condition on the external magnetic field is $(\vec{\nabla} \times \vec{B}^0) \cdot \vec{n} = 0$.

For electrically conducting walls, the magnetic wall boundary condition involves the continuity of the wall-normal magnetic field and the wall-tangent electric field at the fluid-solid interface. By the Ohm’s and Ampère’s laws, and the thin wall approximation, the magnetic boundary condition at a boundary Γ^{cond} reads

$$\vec{B} \cdot \vec{n} = \vec{B}^0 \cdot \vec{n}, \quad (\vec{\nabla} \times \vec{B}) \times \vec{n} = c_d^{-1} (\vec{B}^0 - \vec{B}), \quad \forall \vec{x} \in \Gamma^{\text{cond}}, \quad t \geq 0, \quad (2.26)$$

where $c_d = (\mu_R / \mu_w) d_w$ is a wall conductance coefficient, μ_R is the fluid electrical resistivity introduced in (2.9), μ_w denotes the wall resistivity, and d_w denotes the wall thickness. The wall is assumed to be thin, that is, $d_w \ll L^*$, where L^* is the characteristic length of the domain. The wall conductivity properties are usually expressed in terms of the non-dimensional wall conductance parameter, which is defined as

$$c = \frac{\mu_R d_w}{\mu_w L^*}, \quad (2.27)$$

and, therefore, this non-dimensional quantity expresses the ratio of wall and fluid conductances. For perfectly conducting walls where $c \rightarrow \infty$, the magnetic boundary condition (2.26) reduces to

$$\vec{B} \cdot \vec{n} = \vec{B}^0 \cdot \vec{n}, \quad (\vec{\nabla} \times \vec{B}) \times \vec{n} = \vec{0}, \quad \forall \vec{x} \in \Gamma^{\text{cond}}, \quad t \geq 0, \quad (2.28)$$

and it is valid for walls of any shape and dimension.

For the ideal MHD equations (*i.e.*, system (2.5) with $\vec{\mathbf{f}}^\nu = \vec{\mathbf{0}}$), the wall-normal magnetic field should be zero, *i.e.*, $\vec{B}^0 \cdot \vec{n} = 0$, and the condition on the tangential component of the magnetic field is redundant [30]. In the resistive MHD equations, the wall-normal magnetic field can be nonzero, but the total magnetic flux through any closed surface must be zero due to the divergence-free constraint on the magnetic field. A nonzero wall-normal magnetic field forms a Hartmann boundary layer, which usually requires appropriate mesh refinement for an accurate numerical solution [2].

The GLM term ψ does not require additional boundary conditions at a solid wall. The rationale for this claim is twofold. First, there is no diffusion of ψ in the system. Second, ψ acts as an artificial pressure controlling the divergence of the magnetic field, as described in [19].

2.5. One-dimensional formulation

Following the approach of [18], we reproduce here the system of equations (2.5) in a one-dimensional case. Later on, and for the sake of simplicity, the numerical method will also be formulated in one space dimension.

In one dimension, the GLM-MHD system (2.5) reads

$$\partial_t \mathbf{u} + \partial_x \mathbf{f}^a(\mathbf{u}) + \Upsilon(\mathbf{u}, \vec{\nabla} \mathbf{u}) = \partial_x \mathbf{f}^\nu(\mathbf{u}, \vec{\nabla} \mathbf{u}) + \mathbf{r}. \quad (2.29)$$

Following the notation in [18], we omit the sub-index in the conservative fluxes, \mathbf{f}^a and \mathbf{f}^ν , and in the coordinate, x , to simplify the notation and enhance readability. Thus, we use \mathbf{f}^a , \mathbf{f}^ν , and x instead of \mathbf{f}_1^a , \mathbf{f}_1^ν , and x_1 , respectively. The advective flux in the x direction, split into Euler, MHD, and GLM parts, is given by

$$\mathbf{f}^a = \begin{pmatrix} \rho v_1 \\ \rho v_1^2 + p \\ \rho v_1 v_2 \\ \rho v_1 v_3 \\ v_1 \left(\frac{1}{2} \rho \|\vec{v}\|^2 + \frac{\gamma p}{\gamma - 1} \right) \\ 0 \\ 0 \\ 0 \\ 0 \end{pmatrix} + \begin{pmatrix} 0 \\ \frac{1}{\mu_0} \left(\frac{1}{2} \|\vec{B}\|^2 - B_1^2 \right) \\ -B_1 B_2 / \mu_0 \\ -B_1 B_3 / \mu_0 \\ \frac{1}{\mu_0} \left(v_1 \|\vec{B}\|^2 - B_1 (\vec{v} \cdot \vec{B}) \right) \\ 0 \\ v_1 B_2 - v_2 B_1 \\ v_1 B_3 - v_3 B_1 \\ 0 \end{pmatrix} + \begin{pmatrix} 0 \\ 0 \\ 0 \\ 0 \\ \frac{c_h}{\mu_0} \psi B_1 \\ c_h \psi \\ 0 \\ 0 \\ c_h B_1 \end{pmatrix}. \quad (2.30)$$

The non-conservative term, $\Upsilon = \Upsilon^{\text{MHD}} + \Upsilon^{\text{GLM}}$, consists of the following two parts:

$$\Upsilon^{\text{MHD}} = \frac{\partial B_1}{\partial x} \boldsymbol{\phi}^{\text{MHD}} = \frac{\partial B_1}{\partial x} \begin{pmatrix} 0 \\ B_1/\mu_0 \\ B_2/\mu_0 \\ B_3/\mu_0 \\ \vec{v} \cdot \vec{B}/\mu_0 \\ v_1 \\ v_2 \\ v_3 \\ 0 \end{pmatrix}, \quad \Upsilon^{\text{GLM}} = \frac{\partial \psi}{\partial x} \boldsymbol{\phi}^{\text{GLM}} = \frac{\partial \psi}{\partial x} \begin{pmatrix} 0 \\ 0 \\ 0 \\ 0 \\ v_1 \psi/\mu_0 \\ 0 \\ 0 \\ 0 \\ v_1 \end{pmatrix}. \quad (2.31)$$

The visco-resistive flux in the x direction reads

$$\mathbf{f}^\nu(\mathbf{u}, \vec{\nabla} \mathbf{u}) = \begin{pmatrix} 0 \\ \frac{4}{3} \mu_{NS} \partial_x v_1 \\ \mu_{NS} \partial_x v_2 \\ \mu_{NS} \partial_x v_3 \\ \mu_{NS} \left(\frac{4}{3} v_1 \partial_x v_1 + v_2 \partial_x v_2 + v_3 \partial_x v_3 \right) + \kappa \partial_x T + \frac{\mu_R}{\mu_0^2} (B_2 \partial_x B_2 + B_3 \partial_x B_3) \\ 0 \\ \frac{\mu_R}{\mu_0} \partial_x B_2 \\ \frac{\mu_R}{\mu_0} \partial_x B_3 \\ 0 \end{pmatrix}. \quad (2.32)$$

3. Entropy stable DG-SBP-SAT discretization

This section presents the new discrete entropy conservative and entropy stable solid wall boundary conditions for the GLM-MHD system (2.5). These conditions are compatible with the collocated entropy conservative and entropy stable discontinuous Galerkin (DG) discretization schemes with the summation-by-parts (SBP) property and coupled with simultaneously approximated terms (SAT), (*i.e.*, DG-SBP-SAT operators). The DG-SBP-SAT method was developed and proven to be entropy stable for the GLM-MHD system in unbounded computational domains in [17]. Thus, this work extends the entropy stability proof to include solid wall boundary conditions which can also be “trivially” extended to modal DG-SBP operators.

First, we revisit the method’s definition and entropy stability proof for nodes collocated inside the domain Ω . Then, we introduce the new solid wall boundary conditions and their original proof for the entropy conservation and stability for boundary nodes at a solid wall. We follow the works presented in [20, 21], where discrete entropy-stable solid wall boundary conditions are formulated, verified, and validated for the compressible Navier–Stokes equations. Deviating from the original notation of [17], we introduce a nonsymmetric two-point flux function to address the nonconservative term in the MHD equations. Technically, this approach arises from rearranging terms in the previously introduced expressions. Such rearrangement significantly enhances the clarity of our presentation.

Following the approach outlined in [18], all definitions and proofs are presented for the one-dimensional (1D) case, assuming that all variables vary solely along one spatial coordinate and are uniform in the other two. While the entropy stability of the proposed discrete boundary conditions

are demonstrated in 1D, their formulation is inherently nodal. Therefore, they are applicable across various scenarios where DGSEM is used, including unstructured curvilinear nonconforming meshes with hp -refinement [23, 31].

3.1. DG-SBP-SAT discretization in 1D

To present the DG-SBP-SAT discretization, we rewrite the system of equations (2.29) as a first-order system:

$$\begin{aligned}\partial_t \mathbf{u} + \partial_x \mathbf{f}^a(\mathbf{u}) + \mathbf{\Upsilon}(\mathbf{u}, \partial_x \mathbf{u}) &= \partial_x \mathbf{f}^\nu(\mathbf{u}, \mathbf{g}) + \mathbf{r}(\mathbf{u}), \\ \mathbf{g} &= \partial_x \mathbf{w},\end{aligned}\tag{3.1}$$

where \mathbf{g} denotes the spatial gradient of the entropy variables, \mathbf{w} .

In the case of a 1D problem, the computational mesh is composed of non-overlapping intervals. Each interval is mapped into a reference space, $\xi \in [-1, 1]$. Within each element, all variables are represented using Lagrange interpolating polynomials of degree N , denoted as $\{l_k\}_{k=1}^N$, which are defined on $N + 1$ Legendre–Gauss–Lobatto (LGL) nodes, $\{\xi_k\}_{k=0}^N$. The polynomial basis is continuous within each element but discontinuous at the interfaces between elements. A key aspect for ensuring the entropy conservation property of the scheme is that the undivided derivative matrix, $Q_{jk} = \omega_j D_{jk} = \omega_j l'_k(\xi_j)$, has the SBP property [16, 32], *i.e.*,

$$Q + Q^T = \mathcal{B},\tag{3.2}$$

where ω_j represents the reference space quadrature weight, D_{jk} is the jk element of the one-dimensional (SBP) operator for the first derivative, l'_k indicates the derivative of the k -th Lagrange interpolating polynomial, and \mathcal{B} is a boundary operator defined as

$$\mathcal{B} = \text{diag}(-1, 0, \dots, 0, 1).\tag{3.3}$$

Boundary conditions and conditions at the interfaces between mesh elements are incorporated into the semi-discretization in a weak sense using the simultaneous approximation terms (SATs) approach; see the original SAT works in [33, 34] and its extension to the compressible Navier–Stokes in the context of entropy stability [35]. More details on the method and its extension to multidimensional cases, including the h/p -refinement, can be found in [17, 23, 36].

For the node j in a mesh element, the spatial discretization leads to the following semi-discrete form (*i.e.*, an ordinary differential equation for the unknown vector \mathbf{u}_j),

$$J_j \omega_j \frac{d\mathbf{u}_j}{dt} = -\mathbf{F}_j^a + \mathbf{F}_j^\nu + J_j \omega_j \mathbf{r}_j,\tag{3.4}$$

where J_j is the determinant of the Jacobian of the transformation from the reference space to the physical space, \mathbf{F}_j^a represents the discretization of the advective flux divergence and non-conservative terms combined, \mathbf{F}_j^ν represents the discretization of the diffusive flux divergence, and $\mathbf{r}_j = \mathbf{r}(\mathbf{u}_j)$. Specifically, using a DG-SBP-SAT operator, the discretization of the divergence of the convective flux and the non-conservative term yields

$$\mathbf{F}_j^a = 2 \sum_{k=0}^N Q_{jk} \mathbf{f}_{(j,k)}^* + \delta_{j0} \left(\mathbf{f}_{(0,0)}^* - \mathbf{f}_{(0,L)}^* - \text{DISS}_{(0,L)}^a \right) - \delta_{jN} \left(\mathbf{f}_{(N,N)}^* - \mathbf{f}_{(N,R)}^* + \text{DISS}_{(N,R)}^a \right). \tag{3.5}$$

Here, the index k ranging from 0 to N corresponds to the index of a node within the mesh element. The subscripts L and R refer to the nodes to the “left” and the “right” interface of the “left” and “right” adjacent elements, respectively. These nodes are collocated at the same physical location as those with index $k = 0$ and $k = N$ within the element under consideration and are used to construct the SAT interface terms.

At this point of the section, we depart from the notation used in [17, 18] and introduce a non-symmetric numerical two-point flux function, denoted as $\mathbf{f}_{(j,k)}^* = \mathbf{f}^*(\mathbf{u}_j, \mathbf{u}_k)$. This function is derived by rearranging different terms in the expressions from [18] (specifically, Eq. 32). This step indirectly accounts for the non-conservative term Υ and simplifies the expressions that will follow. The non-symmetric two-point flux is defined as

$$\mathbf{f}^*(\mathbf{u}_i, \mathbf{u}_j) = \mathbf{f}^a(\mathbf{u}_i, \mathbf{u}_j) + \frac{1}{2} (\phi_i^{\text{MHD}} B_{1,j} + \phi_i^{\text{GLM}} \psi_j), \quad (3.6)$$

where $\mathbf{f}^a(\mathbf{u}_i, \mathbf{u}_j)$ represents any symmetric two-point flux function. In our simulations, we use the entropy conservative two-point flux function $\mathbf{f}^{\text{EC}}(\mathbf{u}_i, \mathbf{u}_j)$ designed in [19]. This two-point flux function is reproduced in Appendix A for completeness. The interface dissipation term $\text{DISS}_{(i,j)}^a$ in (3.5) introduces an additional penalty on the solution jump at the mesh element interfaces. The particular form of $\text{DISS}_{(i,j)}^a$ is specified in Section 4.1.

The diffusive term is discretized using a standard SBP differentiation operator constructed at the $N + 1$ LGL points. After some algebraic manipulations and simplifications, the resulting expression for the approximation of the divergence of the diffusive flux reads

$$\mathbf{F}_j^\nu = \sum_{k=0}^N Q_{jk} \mathbf{f}_k^\nu + \delta_{j0} \left(\mathbf{f}_0^\nu - \hat{\mathbf{f}}_{(0,L)}^\nu + \text{DISS}_{(0,L)}^\nu \right) - \delta_{jN} \left(\mathbf{f}_N^\nu - \hat{\mathbf{f}}_{(N,R)}^\nu - \text{DISS}_{(N,R)}^\nu \right), \quad (3.7)$$

where $\mathbf{f}_k^\nu = C^\nu(\mathbf{u}_k) \mathbf{g}_k$ represents the diffusive flux at node k . The discrete gradient of entropy variables, \mathbf{g}_k , is determined using a consistent discretization approach,

$$J_k \omega_k \mathbf{g}_k = \sum_{n=0}^N Q_{kn} \mathbf{w}_n + \delta_{kN} (\hat{\mathbf{w}}_{(N,R)} - \mathbf{w}_N) - \delta_{k0} (\hat{\mathbf{w}}_{(0,L)} - \mathbf{w}_0). \quad (3.8)$$

The diffusive numerical flux $\hat{\mathbf{f}}_{(i,j)}^\nu$ in (3.7) and the numerical entropy variables $\hat{\mathbf{w}}_{(i,j)}$ in (3.8) are computed using the BR1 method [37],

$$\hat{\mathbf{f}}_{(i,j)}^\nu = \frac{1}{2} (\mathbf{f}_i^\nu + \mathbf{f}_j^\nu), \quad \hat{\mathbf{w}}_{(i,j)} = \frac{1}{2} (\mathbf{w}_i + \mathbf{w}_j). \quad (3.9)$$

The visco-resistive interface dissipation $\text{DISS}_{(i,j)}^\nu$ is defined in Section 3.2.

3.2. Entropy conservation for internal nodes

In [17], it is shown that the DG-SBP-SAT method described previously, does not produce or dissipate numerical entropy in internal nodes, *i.e.*, it is entropy conservative when $\text{DISS}^a = \text{DISS}^\nu = 0$, and $\alpha = 0$.¹ This feature can be verified numerically by simulating problems with smooth solutions and periodic computational domain.

¹By internal nodes, we mean nodes lying inside mesh elements or pairs of nodes lying on interfaces between adjacent mesh elements.

The proof of entropy conservation of the interior DG-SBP-SAT operator relies on the generalized Tadmor's condition [17](Eq. 4.8) and [18](Eq. 51), which accounts for the non-conservative contributions. In our notation, the generalized Tadmor's condition reads

$$\mathbf{w}_k^T \mathbf{f}_{(k,j)}^* - \mathbf{w}_j^T \mathbf{f}_{(j,k)}^* = \Psi_k^* - \Psi_j^*, \quad \Psi_k^* = \mathbf{w}_k^T \mathbf{f}_{(k,k)}^* - f_k^S, \quad (3.10)$$

where f_k^S is the entropy flux at the node k . For completeness, we repeat the proof of entropy conservation here. Using condition (3.10) and the SBP property of the differentiation operator encapsulated in (3.2), we next show that the numerical scheme is entropy conservative within a single mesh element. Mimicking the continuous analysis presented in Section 2.3, we contract (3.4) with the entropy variables, \mathbf{w} , on a single mesh element and after some algebraic manipulations and simplifications, we arrive at the following expression

$$\begin{aligned} \frac{d}{dt} \sum_{j=0}^N J_j \omega_j S_j + \sum_{j=0}^N J_j \omega_j \mathbf{g}_j^T \mathbf{C}_j^\nu \mathbf{g}_j + \sum_{j=0}^N J_j \omega_j \frac{\alpha \psi_j^2}{\mu_0 T} = \\ P_{(0,L)}^{\text{a,cons}} + P_{(0,L)}^{\text{a,diss}} + P_{(0,L)}^{\nu,\text{cons}} + P_{(0,L)}^{\nu,\text{diss}} + P_{(N,R)}^{\text{a,cons}} + P_{(N,R)}^{\text{a,diss}} + P_{(N,R)}^{\nu,\text{cons}} + P_{(N,R)}^{\nu,\text{diss}}, \end{aligned} \quad (3.11)$$

where S_j is the entropy function at the node j . Therefore, the discrete entropy within a mesh element changes solely due to the dissipation (second term on the left-hand side), the algebraic damping on ψ (third term on the left-hand side), and the entropy flow across the boundaries of the mesh element (all terms on the right-hand side). In the following expressions, we separate the advective and visco-resistive entropy conservative and dissipative contributions at the left and right boundaries of the mesh element,

$$P_{(0,L)}^{\text{a,cons}} = \left(\mathbf{w}_0^T \mathbf{f}_{(0,L)}^* - \Psi_0^* \right), \quad (3.12)$$

$$P_{(N,R)}^{\text{a,cons}} = - \left(\mathbf{w}_N^T \mathbf{f}_{(N,R)}^* - \Psi_N^* \right), \quad (3.13)$$

$$P_{(0,L)}^{\nu,\text{cons}} = - \left(\hat{\mathbf{w}}_{(0,L)} - \mathbf{w}_0 \right)^T \mathbf{f}_0^\nu - \mathbf{w}_0^T \hat{\mathbf{f}}_{(0,L)}^\nu, \quad (3.14)$$

$$P_{(N,R)}^{\nu,\text{cons}} = \left(\hat{\mathbf{w}}_{(N,R)} - \mathbf{w}_N \right)^T \mathbf{f}_N^\nu + \mathbf{w}_N^T \hat{\mathbf{f}}_{(N,R)}^\nu, \quad (3.15)$$

$$P_{(0,L)}^{\text{a,diss}} = \mathbf{w}_0^T \text{DISS}_{(0,L)}^{\text{a}}, \quad (3.16)$$

$$P_{(N,R)}^{\text{a,diss}} = \mathbf{w}_N^T \text{DISS}_{(N,R)}^{\text{a}}, \quad (3.17)$$

$$P_{(0,L)}^{\nu,\text{diss}} = \mathbf{w}_0^T \text{DISS}_{(0,L)}^\nu, \quad (3.18)$$

$$P_{(N,R)}^{\nu,\text{diss}} = \mathbf{w}_N^T \text{DISS}_{(N,R)}^\nu. \quad (3.19)$$

Next, we demonstrate that the appropriate choice of SAT terms in (3.12) through (3.19) guarantees entropy dissipation at the interfaces between adjacent mesh elements. The scalar equation describing the rate of change of the entropy function in the whole domain is obtained by adding contributions from (3.11) over all the mesh elements. For any node L on the interface between two neighboring mesh elements, a node R exists that belongs to the adjacent element and is spatially coincident with node L . We will separately examine the advective and diffusive fluxes to show that for every L and R node pair, the total entropy production is zero for conservative fluxes and non-positive for entropy dissipative fluxes.

Terms (3.12) and (3.13) are the contributions to the time rate of change of the entropy function due to the advective SATs for the boundary nodes with indices 0 and N . Their cumulative contribution to dS_j/dt is zero, as can be shown by using the generalized Tadmor's condition (3.10):

$$\frac{dS_{L+R}^{a,\text{cons}}}{dt} = \left(\mathbf{w}_R^T \mathbf{f}_{(R,L)}^* - \Psi_R^* \right) - \left(\mathbf{w}_L^T \mathbf{f}_{(L,R)}^* - \Psi_L^* \right) = \left(\mathbf{w}_R^T \mathbf{f}_{(R,L)}^* - \mathbf{w}_L^T \mathbf{f}_{(L,R)}^* \right) - (\Psi_R^* - \Psi_L^*) = 0.$$

The dissipation operator DISS^a is antisymmetric in its arguments and can be expressed as a linear operator on the jump in the entropy variables,

$$\text{DISS}_{(i,j)}^a = \hat{D} \llbracket \mathbf{w} \rrbracket_{(i,j)}, \quad (3.20)$$

where \hat{D} is a symmetric positive semi-definite matrix. Thus, with the definition (3.20), the (numerical) contribution to the time rate of change of the entropy function due to the terms (3.16) and (3.17) is given by

$$\frac{dS_{L+R}^{a,\text{diss}}}{dt} = \mathbf{w}_R^T \text{DISS}_{(R,L)}^a + \mathbf{w}_L^T \text{DISS}_{(L,R)}^a = -\llbracket \mathbf{w} \rrbracket_{(L,R)}^T \hat{D} \llbracket \mathbf{w} \rrbracket_{(L,R)},$$

which is negative due to the positive semi-definiteness of \hat{D} .

Similar to the above reasoning, using the expressions given in (3.9), we can show that the cumulative contribution to the time derivative of the entropy function due to the entropy conservative visco-resistive part of the flux expressed by (3.14) and (3.15) is zero,

$$\frac{dS_{L+R}^{\nu,\text{cons}}}{dt} = (\hat{\mathbf{w}}_{(L,R)} - \mathbf{w}_L)^T \mathbf{f}_L^\nu - (\hat{\mathbf{w}}_{(R,L)} - \mathbf{w}_R)^T \mathbf{f}_R^\nu + \mathbf{w}_L^T \hat{\mathbf{f}}_{(L,R)}^\nu - \mathbf{w}_R^T \hat{\mathbf{f}}_{(R,L)}^\nu = 0. \quad (3.21)$$

Finally, we consider the contribution of the visco-resistive operator DISS^ν , which reads

$$\text{DISS}_{(i,j)}^\nu = \hat{L} \llbracket \mathbf{w} \rrbracket_{(i,j)}, \quad \hat{L} = \beta \frac{C_i^\nu + C_j^\nu}{2}, \quad \beta \geq 0, \quad (3.22)$$

where \hat{L} is a scaled average matrix between the two symmetric positive semi-definite dissipation matrices $C_i^\nu = C_{11}^\nu(\mathbf{u}_i)$ and $C_j^\nu = C_{11}^\nu(\mathbf{u}_j)$ defined in (2.20). The nonnegative coefficient β modulates the strength of the dissipation term. Therefore, the contribution to the time rate of change of the entropy function due to the (numerical) visco-resistive dissipative mechanisms is

$$\frac{dS_{L+R}^{\nu,\text{diss}}}{dt} = \mathbf{w}_L^T \text{DISS}_{(L,R)}^\nu + \mathbf{w}_R^T \text{DISS}_{(R,L)}^\nu = -\llbracket \mathbf{w} \rrbracket_{(L,R)}^T \hat{L} \llbracket \mathbf{w} \rrbracket_{(L,R)},$$

which is nonpositive due to the definition of \hat{L} .

In the following section, we introduce the discrete boundary conditions for the advective and the visco-resistive terms, which guarantees a physically consistent production of the discrete entropy function in a bounded domain.

4. Entropy conservative solid wall boundary conditions

We consider boundary nodes within the computational domain corresponding to the internal fluid state and denote any of such nodes as $(-)$.² Each node $(-)$ lies (conceptually) on one side

²At the boundary, we switch from the notation L , R to $(-)$, $(+)$ to define internal and corresponding ghost external nodes.

of the element boundary face and has a corresponding virtual or ghost node, denoted as $(+)$, which spatially coincides with node $(-)$ but lies (conceptually) on the opposite side of the face. Our objective is to define manufactured quantities at the ghost node $(+)$ as a function of the discrete state and its gradient at node $(-)$ and the boundary conditions data such that i) the resulting boundary conditions imposition is entropy conservative or entropy stable and ii) the same discretization procedure used to treat internal interfaces between mesh elements can be used to impose boundary conditions. The latter objective has also been one of the guiding principles in the construction of the entropy conservative and entropy stable solid wall boundary conditions presented in [20].

Similarly to the approach proposed in [20, 21] for the compressible Navier–Stokes equations, we must ensure that the discrete imposition of the solid wall boundary conditions for the GLM-MHD system (2.5) leads to an appropriate and physically consistent entropy production or dissipation.

4.1. Advective numerical flux divergence operator

Herein, boundary conditions are formulated in primitive variables, defined by letter \mathbf{v} . The following theorem defines the manufactured state $\mathbf{v}_{(+)}^a$ to be substituted into the advective numerical flux $\mathbf{f}^*(\mathbf{v}_{(-)}, \mathbf{v}_{(+)})$ and advective dissipation $\text{DISS}^a(\mathbf{v}_{(-)}, \mathbf{v}_{(+)})$ in expression (3.5). We define the manufactured state in the proper and general three-dimensional setting, while the proof is carried out under the one-directional assumption for simplicity. In our notation, we omit the subscript $(-)$ on the individual components of the state $\mathbf{v}_{(-)} = (\rho, \vec{v}, T, \vec{B}, \psi)^T$, to improve readability.

Theorem 3. *The advective flux penalty term, disregarding any contributions from the advective dissipation operator DISS^a , is entropy-conservative if the vector boundary state is defined in primitive variables as*

$$\mathbf{v}_{(+)}^a = \begin{bmatrix} \rho \\ \vec{v} - 2(\vec{v} \cdot \vec{n})\vec{n} \\ T \\ \vec{B} - 2(\vec{B} \cdot \vec{n} - \vec{B}^0 \cdot \vec{n})\vec{n} \\ \psi \end{bmatrix}. \quad (4.1)$$

PROOF. Without loss of generality, we assume that node $(-)$ is assigned the index N within its mesh element. In this context, the ‘right’ node is node $(+)$ and the entropy produced at this node by the advective operator \mathbf{F}^a , disregarding the contribution from the advective dissipation operator DISS^a , corresponds to (3.13); direct substitution of (4.1) into (3.13) with the proper node index substitutions yields

$$\frac{dS_{(-)}^{a,\text{cons}}}{dt} = -\left(\mathbf{w}_{(-)}^T \mathbf{f}^*(\mathbf{u}_{(-)}, \mathbf{u}_{(+)}) - \Psi_{(-)}^*\right) = 0, \quad (4.2)$$

which proves the theorem. \square

Now, we examine the effect of the dissipation operator DISS^a applied to the solution jump at the boundary. We consider the local Lax-Friedrichs (LLF) dissipation, modified to act in entropy space,

$$\text{DISS}_{(i,j)}^{a,\text{LLF}} = \frac{1}{2}|\lambda|_{\max} \underline{\mathcal{H}}[\mathbf{w}]_{(i,j)}, \quad (4.3)$$

where $|\lambda|_{\max}$ is the maximum absolute eigenvalue of the flux Jacobian considering both the i and j states, and the transformation matrix $\underline{\mathcal{H}}$ is a numerical analog of the continuous matrix $\mathcal{H} = \partial \mathbf{u} / \partial \mathbf{w}$

presented in [Appendix B](#). Our proof is quite general and allows for several possible definitions of $\underline{\mathcal{H}}$. As one possibility, $\underline{\mathcal{H}} = \mathcal{H}(\bar{\mathbf{u}})$ can be evaluated at some average state $\bar{\mathbf{u}} = \bar{\mathbf{u}}(\mathbf{u}_i, \mathbf{u}_j)$. Another option, proposed in [\[38\]](#), defines $\underline{\mathcal{H}} = \mathcal{H}(\mathbf{u}_i, \mathbf{u}_j)$ to be symmetric positive semi-definite and satisfying the condition $\llbracket \mathbf{u} \rrbracket = \underline{\mathcal{H}} \llbracket \mathbf{w} \rrbracket$ in all variables except energy to negotiate the difference between the LLF operators applied in conservative and entropy spaces. In both cases, the entries of $\underline{\mathcal{H}}$ result from some averaging procedure between states i and j denoted here with an overline. The following theorem substantiates the restriction on the average procedure, guaranteeing entropy stability of the LLF dissipation operator at the boundary.

Theorem 4. *The local Lax-Friedrich dissipation operator (4.3) with the boundary state (4.1) is entropy stable at the boundary if in the definition of the matrix $\underline{\mathcal{H}}$, the average state $\bar{\mathbf{u}}$ satisfies*

$$\bar{v}_n = 0, \quad \bar{B}_n = B_n^0, \quad \bar{T} > 0, \quad \bar{\rho} > 0, \quad (4.4)$$

where \bar{v}_n and \bar{B}_n are the normal components of the corresponding average vectors.

PROOF. Without loss of generality, we assume that the node $(-)$ has index N inside the mesh element. In this context, the ‘right’ node is denoted by $(+)$ and the dissipative part of the advective entropy flux defined by (3.17) relies on the computation of LLF operator (4.3). The jump in entropy variables at the boundary has only two non-zero components:

$$\llbracket \mathbf{w} \rrbracket_{(-),(+)} = \left[0, -\frac{2v_1}{T}, 0, 0, 0, \frac{2(B_1^0 - B_1)}{\mu_0 T}, 0, 0, 0 \right]^T. \quad (4.5)$$

Therefore, we represent here only the two columns of matrix $\underline{\mathcal{H}}$, interacting with the nonzero elements in (4.5). Under the assumption (4.4), the dissipative term equals

$$\text{DISS}_{(-),(+)}^{a,\text{LLF}} = \frac{1}{2} |\lambda|_{\max} \underline{\mathcal{H}} \llbracket \mathbf{w} \rrbracket_{(-),(+)} = \frac{1}{2} |\lambda|_{\max} \begin{bmatrix} 0 & 0 \\ \bar{\rho} \bar{T} & 0 \\ 0 & 0 \\ 0 & 0 \\ 0 & \bar{T} B_1^0 \\ 0 & \bar{T} \mu_0 \\ 0 & 0 \\ 0 & 0 \\ 0 & 0 \end{bmatrix} \begin{bmatrix} -2v_1/T \\ 2(B_1^0 - B_1)/\mu_0 T \end{bmatrix}. \quad (4.6)$$

At the boundary node, the contribution of the LLF dissipation operator to the time derivative of the global entropy function of the system is expressed by using (4.3) in (3.17) with corresponding substitution of indexes,

$$\frac{dS_{(-)}^{a,\text{LLF}}}{dt} = \mathbf{w}_{(-)}^T \text{DISS}_{(-),(+)}^{a,\text{LLF}} = -|\lambda|_{\max} \frac{\bar{T}}{T^2} \left(\bar{\rho} v_1^2 + \frac{(B_1^0 - B_1)^2}{\mu_0} \right). \quad (4.7)$$

Positivity of the average density $\bar{\rho}$ and temperature \bar{T} guarantees nonpositivity of the expression (4.7) and thus the entropy stability of the LLF operator. \square

Both the LLF dissipation operator defined in [\[19\]](#) or the LLF operator defined from the simple arithmetic average between two states satisfy the conditions of Theorem 4. Therefore, we attain entropy stability at the boundary and interior nodes.

4.2. Diffusive numerical flux divergence operator

In the analysis of the visco-resistive term, we need to define not only the manufactured state $\mathbf{v}_{(+)}^\nu$, but also the manufactured gradient of entropy variables $\mathbf{g}_{(+)}$ at the ghost node (+), both to be substituted in expressions (3.7) and (3.8). Since our solid wall boundary conditions involve conditions on gradients of primitive variables, we need a transformation procedure to go back and forth between gradients of primitive and entropy variables. The procedure adopted in this work is as follow [20, 21],

1. From the known gradient of entropy variables $\mathbf{g}_{(-)}$, we compute the gradient of primitive variables $\boldsymbol{\theta}_{(-)}$ by multiplying $\mathbf{g}_{(-)}$ with the Jacobian matrix of the variable transformation $\mathbf{w} \rightarrow \mathbf{v}$ computed at the internal state $\mathbf{v}_{(-)}$,

$$\boldsymbol{\theta}_{(-)} = \left[\frac{\partial \mathbf{v}}{\partial \mathbf{w}} \right]_{(-)} \mathbf{g}_{(-)}. \quad (4.8)$$

2. From the gradient of primitive variables $\boldsymbol{\theta}_{(-)}$, we define the manufactured gradient of primitive variables $\boldsymbol{\theta}_{(+)}$ at the ghost node. Definitions for the components of $\boldsymbol{\theta}_{(+)}$ in terms of those of $\boldsymbol{\theta}_{(-)}$ and local state $\mathbf{v}_{(-)}$ are specified in Theorems 5 and 6 presented next.
3. From the gradient of primitive variables $\boldsymbol{\theta}_{(+)}$, we compute the gradient of entropy variables $\mathbf{g}_{(+)}$ by multiplying $\boldsymbol{\theta}_{(+)}$ with the Jacobian matrix of the variable transformation $\mathbf{v} \rightarrow \mathbf{w}$ computed at the manufactured state vector $\mathbf{v}_{(+)}^\nu$,

$$\mathbf{g}_{(+)} = \left[\frac{\partial \mathbf{w}}{\partial \mathbf{v}} \right]_{(+)} \boldsymbol{\theta}_{(+)}. \quad (4.9)$$

We first restrict our analysis to the case $\text{DISS}^\nu = 0$ and show the entropy conservative properties of the manufactured boundary state. Without loss of generality, we assume that the boundary node $(-)$ has index N and lies within the rightmost mesh element, while the ghost node $(+)$ is to the right of node $(-)$. Thus, with the particular form of boundary fluxes (3.9), the contribution of the diffusive dissipation term (3.15) to the time derivative of the discrete entropy function reads

$$\frac{dS_{(-)}^{\nu, \text{cons}}}{dt} = (\hat{\mathbf{w}}_{(-),(+)} - \mathbf{w}_{(-)})^T \mathbf{f}_{(-)}^\nu + \mathbf{w}_{(-)}^T \hat{\mathbf{f}}_{(-),(+)}^\nu = \frac{1}{2} \left(\mathbf{w}_{(+)}^T \mathbf{f}_{(-)}^\nu + \mathbf{w}_{(-)}^T \mathbf{f}_{(+)}^\nu \right). \quad (4.10)$$

Guided by Theorem 2, we define the manufactured state $\mathbf{w}_{(+)}^\nu$ and the gradient $\mathbf{g}_{(+)}^\nu$ such that the boundary diffusive flux, $\mathbf{f}_{(+)}^\nu = C_{(+)}^\nu \mathbf{g}_{(+)}^\nu$, satisfies the condition

$$\frac{1}{2} \left(\mathbf{w}_{(+)}^T \mathbf{f}_{(-)}^\nu + \mathbf{w}_{(-)}^T \mathbf{f}_{(+)}^\nu \right) = g(t). \quad (4.11)$$

We consider two different cases. The first one covers electrically insulating walls, cf. (2.25). The second one covers the electrically conducting walls, cf. (2.26). Boundary conditions for the velocity and temperature follows (2.23), (2.24). In the following theorems, we define manufactured states and gradients in the proper and general three-dimensional setting, while the proofs are carried out under the one-directional assumption for simplicity. In our notation, we omit the subscript $(-)$ on the individual components of the state $\mathbf{v}_{(-)} = (\rho, \vec{v}, T, \vec{B}, \psi)^T$, and gradient $\boldsymbol{\theta}_{(-)}^T = (\theta_{(\rho)}^T, \theta_{(\vec{v})}^T, \theta_{(T)}^T, \theta_{(\vec{B})}^T, \theta_{(\psi)}^T)$, where $\theta_{(\cdot)}$ refers to the gradient components corresponding to a particular set of primitive variables.

The following theorem proposes the manufactured state and gradient for electrically insulating walls.

Theorem 5. *For electrically insulating walls and disregarding the interface dissipation operator DISS^ν , the manufactured state and gradient*

$$\mathbf{v}_{(+)}^{\nu, \text{ins}} = \begin{bmatrix} \rho \\ -\vec{v} + 2\vec{v}^w \\ T \\ -\vec{B} + 2\vec{B}^0 \\ \psi \end{bmatrix}, \quad \boldsymbol{\theta}_{(+)}^{\text{ins}} = \begin{bmatrix} -\theta_{(\rho)} \\ \theta_{(\vec{v})} \\ -\theta_{(T)} + 2\kappa^{-1}Tg(t)\vec{n} \\ \theta_{(\vec{B})} \\ -\theta_{(\psi)} \end{bmatrix} \quad (4.12)$$

guarantee that the penalty terms for the diffusive flux, together with the penalty on the gradient of the entropy variables, are

- entropy conservative if the wall is adiabatic, that is $g(t) = 0$,
- entropy stable in the presence of a heat entropy flux, that is $g(t) \neq 0$, where $g(t)$ is a given L^2 function.

PROOF. Direct substitution of (4.12) into (4.10) satisfies the condition (4.11). If the heat entropy flux $g(t) = 0$, the contribution to the discrete entropy is zero, and the scheme is entropy conservative. If the heat entropy flux $g(t)$ is a given L^2 function, only a bounded amount of discrete entropy enters the domain at node $(-)$ during any time interval $[0, t]$. Thus, summing up all the contributions from all boundary nodes yields a bounded contribution to the time derivative of the discrete entropy function in the system at any time t . \square

The following theorem proposes the manufactured state and gradient for the electrically conducting walls. An additional motivation for the proposed manufactured state for the magnetic component given in this theorem is presented in [Appendix C](#).

Theorem 6. *For electrically conducting walls and disregarding interface dissipation operator DISS^ν , the manufactured state and gradient*

$$\mathbf{v}_{(+)}^{\nu, \text{cond}} = \begin{bmatrix} \rho \\ -\vec{v} + 2\vec{v}^w \\ T \\ \vec{B} \\ \psi \end{bmatrix}, \quad \boldsymbol{\theta}_{(+)}^{\text{cond}} = \begin{bmatrix} -\theta_{(\rho)} \\ \theta_{(\vec{v})} \\ -\theta_{(T)} + 2\kappa^{-1}Tg(t)\vec{n} \\ \theta_{(\vec{B})}^T + 2c_d^{-1}(\vec{B}^0 - \vec{B})^T\vec{n} \\ -\theta_{(\psi)} \end{bmatrix}, \quad (4.13)$$

guarantee that the penalty terms for the visco-resistive flux, together with the penalty on the gradient of the entropy variables, are

- entropy conservative if the wall is adiabatic, that is $g(t) = 0$,
- entropy stable in the presence of a heat entropy flux, that is $g(t) \neq 0$, where $g(t)$ is a given L^2 function.

PROOF. Direct substitution of (4.13) into (4.10) satisfies the condition (4.11). If the heat entropy flux is zero, i.e., $g(t) = 0$, the contribution to the time derivative of the discrete entropy function is zero, and the scheme is entropy conservative. If the heat entropy flux, $g(t)$, is a nonzero function in L^2 , only a bounded amount of discrete entropy enters the domain at node $(-)$ during any time interval $[0, t]$. Therefore, summing up all the contributions from all boundary nodes leads to a bounded contribution to the time derivative of the discrete entropy function in the system at any time t . \square

Finally, we examine the visco-resistive interface dissipation DISS^ν defined in (3.22). The following theorem proves that this operator leads to discrete entropy dissipation.

Theorem 7. *The visco-resistive dissipation operator DISS^ν , defined in (3.22), with either boundary state and gradient (4.12) or (4.13), is entropy dissipative at boundary nodes.*

PROOF. Without loss of generality, we assume that the node $(-)$ has index N and lies within the rightmost mesh element, while the ghost node $(+)$ is to the right of node $(-)$. Under this assumption, and with the corresponding substitution of indices, the visco-resistive dissipation operator DISS^ν contributes to the discrete entropy through the term (3.19).

For the insulating wall case, direct substitution of the boundary state and gradient (4.12) into (3.19) simplifies to

$$\begin{aligned} \frac{d}{dt} S_{(-)}^{\nu, \text{diss}, \text{ins}} &= \mathbf{w}_{(-)}^T \text{DISS}_{(-), (+)}^{\nu, \text{ins}} = \\ &= -\frac{2\beta}{T} \left[\mu_{\text{NS}} \left(\frac{4}{3} v_1^2 + (v_2^{\text{w}} - v_2)^2 + (v_3^{\text{w}} - v_3)^2 \right) + \frac{\mu_R}{\mu_0^2} \left((B_2^0 - B_2)^2 + (B_3^0 - B_3)^2 \right) \right], \end{aligned} \quad (4.14)$$

which is non positive for a positive temperature, T , and positive values of β , μ_{NS} , and μ_R .

For the conducting wall case, direct substitution of boundary state and gradient (4.13) into (3.19) simplifies to

$$\frac{d}{dt} S_{(-)}^{\nu, \text{diss}, \text{cond}} = \mathbf{w}_{(-)}^T \text{DISS}_{(-), (+)}^{\nu, \text{cond}} = -\frac{2\beta\mu_{\text{NS}}}{T} \left(\frac{4}{3} v_1^2 + (v_2^{\text{w}} - v_2)^2 + (v_3^{\text{w}} - v_3)^2 \right), \quad (4.15)$$

which is also non positive under the same conditions for T , β , and μ_{NS} . \square

Remark 2. *The visco-resistive flux does not depend on ρ , ψ , and their gradients. Therefore, it is not strictly necessary to specify them in the manufactured states and gradients (4.12) or (4.13). Nonetheless, the complete specification may be helpful in the case of using unconventional diffusive fluxes arising from alternative physical models. See [39, 40] for an example of the use of alternative viscous fluxes including mass diffusion under an unifying mechanism for the mass/momentum/energy diffusive processes.*

5. Numerical results

In this section, we preset numerical results to demonstrate the accuracy and reliability of the developed boundary conditions for the DG-SBP-SAT discretization operators.

The unstructured grid solver SSDC [41] used herein has been developed at KAUST. The solver is built on top of the Portable and Extensible Toolkit for Scientific Computing (PETSc) [42], its mesh topology abstraction (DMplex) [43] and scalable ordinary differential equation (ODE)/differential algebraic equations (DAE) solver library [44], and the Message Passing Interface (MPI). The SSDC solver is also based on various algorithms for interior operators, [16, 22, 23, 35, 45] boundary nodes treatments that preserve the accuracy of the interior operators [20, 21], and time integration techniques [46–48] It uses a transformation from computational to physical space that satisfies both the entropy conservation and the geometric conservation law at the semi-discrete level [49, 50]. The

computational meshes are generated with Gmsh [51]. Figures are created using Matplotlib [52] and ParaView [53].

SSDC solves the governing equations (2.5) in non-dimensional form. In the following, dimensionless quantities are denoted with a prime, and (dimensional) reference quantities are denoted with an asterisk. The independent reference quantities are defined as follows,

$$\begin{aligned} L^* \vec{x}' = \vec{x}, \quad U^* \vec{v}' = \vec{v}, \quad \rho^* \rho' = \rho, \quad T^* T' = T, \quad B^* \vec{B}' = \vec{B}, \\ R^* R' = R, \quad \mu_{NS}^* \mu_{NS}' = \mu_{NS}, \quad \kappa^* \kappa' = \kappa, \quad \mu_R^* \mu_R' = \mu_R, \end{aligned} \quad (5.1)$$

where L^* is the reference length scale, U^* is the reference velocity, ρ^* is the reference density, T^* is the reference temperature, B^* is the reference magnetic field magnitude, R^* is the reference gas constant, μ_{NS}^* is the reference dynamic viscosity, κ^* is the reference thermal conductivity, and μ_R^* is the reference electric resistivity of the system. In all examples in this section, the properties of the gas are assumed constant and equal to the respective reference values such that $R' = \mu_{NS}' = \kappa' = \mu_R' = 1$. Substitution of (5.1) into the governing equations (2.5) results into the following six non-dimensional numbers

$$\gamma = \frac{C_p}{C_v}, \quad (\text{Heat capacity ratio}) \quad (5.2)$$

$$\text{Ma} = \frac{U^*}{\sqrt{\gamma R^* T^*}}, \quad (\text{Gasdynamic Mach number}) \quad (5.3)$$

$$\text{Re} = \frac{L^* U^* \rho^*}{\mu_{NS}^*}, \quad (\text{Hydrodynamic Reynolds number}) \quad (5.4)$$

$$\text{Pr} = \frac{C_p \mu_{NS}^*}{\kappa^*}, \quad (\text{Prandtl number}) \quad (5.5)$$

$$\text{M}_m = \frac{U^* \sqrt{\mu_0 \rho^*}}{B^*}, \quad (\text{Magnetic or Alfvén Mach number}) \quad (5.6)$$

$$\text{R}_m = \frac{\mu_0 U^* L^*}{\mu_R}, \quad (\text{Magnetic Reynolds number}) \quad (5.7)$$

where the heat capacities at constant pressure (C_p) and volume (C_v) are assumed to be constant. Other non-dimensional quantities can be defined with the independent reference quantities from (5.1), including

$$t' = \frac{L^*}{U^*} t, \quad E' = \frac{E}{\rho^* \gamma C_v T^*}, \quad F' = \frac{L^*}{\rho^* U^{*2}} F, \quad \psi' = \frac{\psi}{B^*}, \quad c_h' = \frac{c_h}{U^*}, \quad \alpha' = \frac{L^*}{U^*} \alpha, \quad (5.8)$$

where F is an external forcing required later for the specification of one of our proposed test cases.

Unless otherwise stated, we define the damping parameter α' as a multiple of the hyperbolic divergence cleaning speed c_h' , in particular we use $\alpha' = c_h'/0.18$ following recommendations from [19, 26]. The value of c_h' is chosen on a case-by-case basis so that it does not negatively impact time step size. Unless otherwise stated, the local Lax–Friedrichs dissipation [54] and the visco-resistive dissipation from 3.22 are applied to mesh element interfaces.

For integration in time, we use the fourth-order accurate Dormand–Prince method [55] adjusted with the adaptive time-stepping technique based on the digital signal processing [56–58].

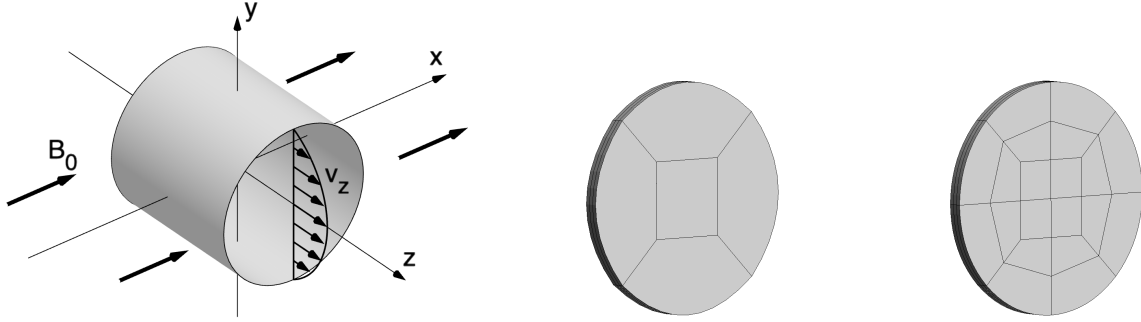


Figure 1: Convergence study: schematic, base hexahedral mesh, and the first level of mesh refinement for the pipe flow.

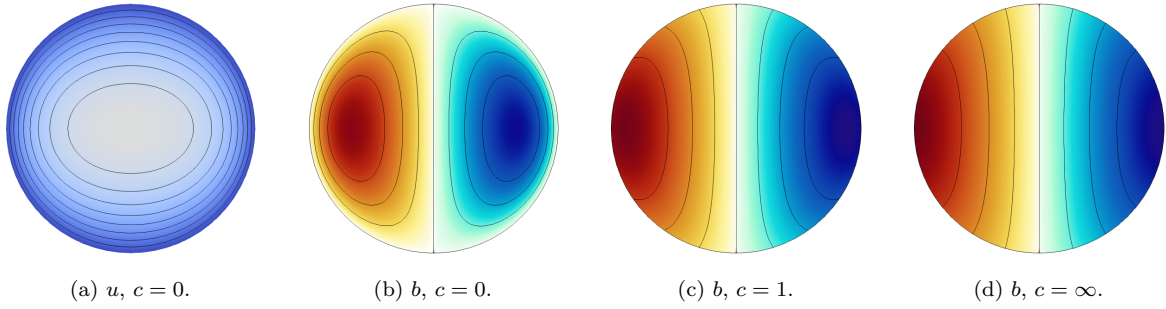


Figure 2: Axial velocity, u' , and magnetic field, b' , in a pipe at three different values of the wall conductance parameter, $c = 0, 1, \infty$, at $Ha = 5$. Due to the slight dependence of u' on c at $Ha = 5$, only the plot for u' at $c = 0$ is shown.

5.1. Convergence study

In this section, we verify the accuracy of the proposed discrete boundary conditions. As a test problem, we consider the flow of an electrically conducting fluid in a circular pipe under an external transverse uniform magnetic field and an external uniform force in the axial direction driving the fluid movement. In the incompressible limit, this problem has a steady-state analytical solution expressed in terms of modified Bessel functions of the first kind [59]. The solution is reproduced in [Appendix D](#) for completeness.

The flow domain is oriented such that the z -axis coincides with the longitudinal axis of a pipe of radius a and the x -axis is aligned with an external magnetic field of strength B_0 (see [Figure 1](#)). The analytical solution takes the form

$$\vec{v} = [0, 0, u(x, y)], \quad \vec{B} = [B_0, 0, b(x, y)],$$

and it is compatible with the boundary conditions defined in [Section 2.4](#). Up to scaling factors depending on the external force and the Reynolds number, the solution essentially depends on two non-dimensional parameters: the wall conductance parameter c defined in [\(2.27\)](#) with $L^* = a$ and the Hartmann number Ha ; see [Appendix D](#) for additional details.

We study three different cases for the wall conductance parameter: $c = 0$, corresponding to an electrically insulating wall, $c = 1$, corresponding to an electrically conducting wall, and $c = \infty$, corresponding to an electrically perfectly conducting wall. The first case tests the electrical insulating properties of the discrete wall boundary conditions [\(4.12\)](#), while the other two test the

electric conductivity properties of the discrete wall boundary conditions (4.13). In all cases, the Hartmann number is set to $\text{Ha} = 5$. At this value of the Hartmann number, electromagnetic forces are strong enough to deflect the axial velocity distribution from an axisymmetric parabolic profile, while the Hartman boundary layer is still thick enough to allow for the use of relatively coarse meshes as needed in a convergence study.

The resulting axial velocity and magnetic field distributions are plotted in Figure 2. The conducting fluid moving in the magnetic field produces an electric current that flows along the iso-lines of the axial magnetic field, $b(x, y)$. This electric current interacts with the magnetic field to produce a Lorentz force, which affects the velocity profile and exhibits anisotropy in the direction of x vs. y . Constant velocity contours expand from the center and compress towards the boundary in the x -direction along the external magnetic field. In the case of an electrically insulating wall, the iso-lines of the magnetic field do not intersect the boundary, which is consistent with no electric current flowing through the wall. In the case of a perfectly conducting wall, the iso-lines of the magnetic field intersect the boundary at right angles, which is consistent with the electric current flowing through the wall only in the wall-normal direction.

To obtain an accurate numerical solution for the incompressible equations using a compressible solver, a small enough Mach number is required to achieve convergence. An incompressible hydrodynamic Poiseuille flow solution and a uniform magnetic field are used as initial conditions. The Mach number is progressively decreased in three stages: $\text{Ma} = 10^{-2}, 10^{-3}, 10^{-4}$. At each stage, the solution is evolved to a steady state. A Reynolds number $\text{Re} = 1$ guarantees that this test will validate both viscous and advective parts of the boundary conditions. The hyperbolic divergence cleaning speed c'_h is of the same order as the maximum characteristic speed in the system but less than it to not affect the size of time step, $c'_h = \text{Ma}^{-1}$. We assume the wall to be adiabatic. Therefore, extra effort is needed to remove the heat generated by viscous and resistive mechanisms. To this end, and to accelerate the decay of perturbations in the pressure field, we applied to the energy equation damping mechanism similar to the one used for the generalized Lagrange multiplier ψ , and then we redefine the damping term in (2.5) to the following non-dimensional form

$$\mathbf{r}' = [0, \vec{0}, -\alpha'_1 \rho'_0 \gamma^{-1} (T' - T'_0), \vec{0}, -\alpha'_2 \psi']^T, \quad (5.9)$$

where T'_0 and ρ'_0 are undisturbed, reference non-dimensional temperature and density in the flow. Following the recommendations in [19, 26], we set $\alpha'_1 = \text{Ma}^{-1}/0.18$, $\alpha'_2 = c'_h/0.18$ in all cases. All the other parameters are defined from the Hartman number Ha and wall conductance parameter c as detailed in Appendix D.

For the convergence study, we compute the discrete L_2 norm or the error between the analytical and numerical solutions

$$\|e\|_{L_2} = \|\Omega\|^{-1} \left[\sum_{k=1}^K J_k \omega_k e_k^2 \right]^{1/2}, \quad (5.10)$$

where the index k spans all nodes in the computational domain, $\|\Omega\|$ indicates the volume of the computational domain, J_k is the determinant of the Jacobian of the transformation from physical to computational space, ω_k is the quadrature weight in computational space, and e_k is the difference between the analytical and numerical solutions at the node k .

The convergence study is performed using a sequence of nested three-dimensional butterfly-type hexahedral meshes. The base mesh and the first level of refinement are shown in Figure 1. The length along the axial direction is equal to the $1/8$ of the pipe radius and is discretized with three

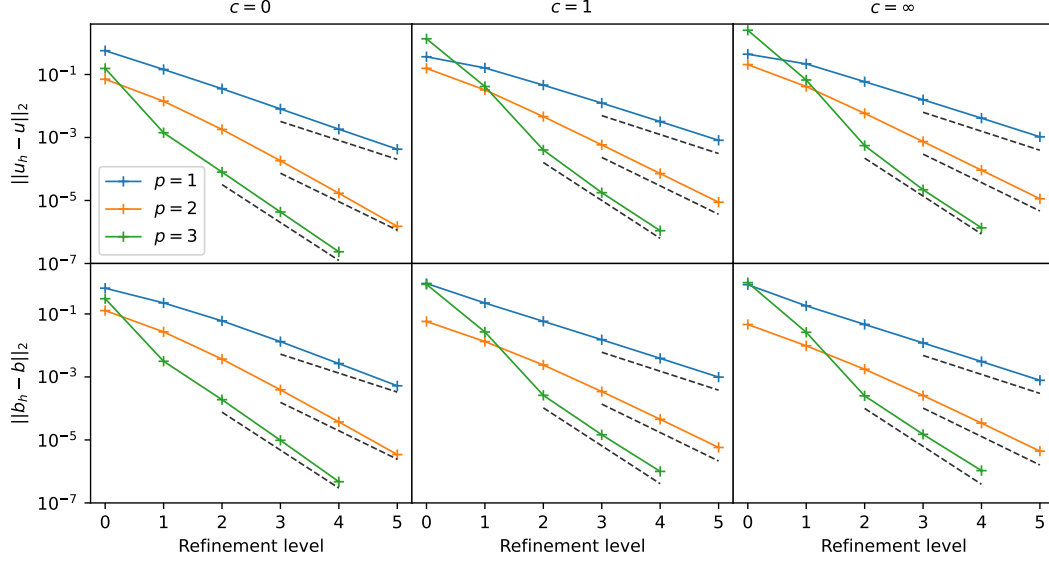


Figure 3: Convergence study for pipe flow with solution polynomial degrees $p = 1, 2, 3$; wall conductance parameter $c = 0, 1, \infty$; $\text{Ha} = 5$. L_2 errors in axial velocity u and axial magnetic field b compared to the analytical solution are shown with the “expected” convergence rates $\mathcal{O}(h^{p+1})$ (dashed lines). At a generic refinement level l , the mesh has $5 \cdot 4^l$ elements in cross-section; in the axial direction number of elements is constant and equals 3. The raw convergence data used for these plots is available in Table E.1.

mesh elements for all levels of refinement. The base mesh has five elements in the cross-section. Each level of uniform mesh refinement splits each hexahedral cell into four new cells in the cross-section. The meshes have curved boundary element faces to accurately approximate the cylindrical wall geometry using a polynomial degree that matches the solution polynomial order. In all cases, we use absolute and relative tolerance of 10^{-11} for the adaptive time-stepping scheme to guarantee the local truncation error in time is negligible compared to the space discretization error.

The results for the second, third, and fourth-order approximation of the numerical solution, corresponding to $p = 1, 2, 3$ polynomial degrees and $N = 2, 3, 4$ LGL nodes in each coordinate direction, are shown in Figure 3, where each column corresponds to different values of c . For each value of c , the plot shows the L_2 error of the axial velocity and axial magnetic field – these are the only two solution components deviating from a uniform value in the analytical solution. In all cases, the convergence rate reaches the “expected” value of $p + 1$ (dashed lines). The various data points from Figure 3 are also available in the appendix in Table E.1. The two worst numbers are -3.87 and -3.93 achieved with $p = 3$ at the 4-th level of refinement for the magnetic field with conducting boundary, which can be rationalized by the super-convergence rates achieved for the same variables at the previous levels of refinement.

5.2. Entropy conservation study

This test case is designed to verify the entropy conservative properties of the spatial discretization algorithm and our proposed hydrodynamic, thermal, and magnetic boundary conditions. As shown in Figure 4, the computational domain has an exterior cubic shape. Within the cube’s interior, the plasma is set in motion by the rotation of an spheroidal solid body around its major

axis, which is aligned with one of the long diagonals of the cube. An external magnetic field is generated by a magnetic dipole located within the spheroid. The dipole axis matches the minor axis of the spheroid and rotates with it; this way, the external magnetic field varies with time.

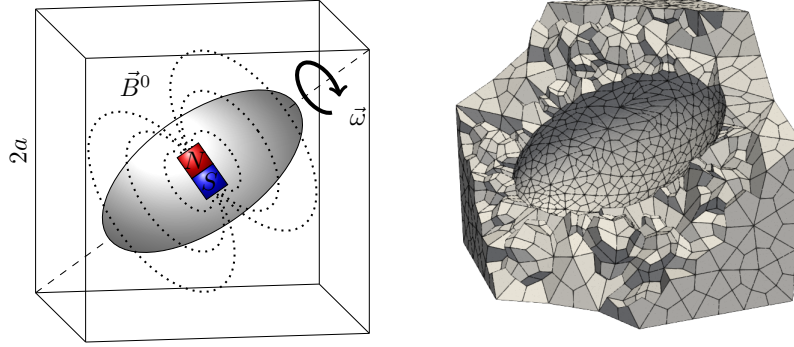


Figure 4: Discrete entropy conservation test: schematic of the domain and computational mesh for the spinning spheroid.

In Cartesian coordinates the plasma fills the interior of the cube of edge length $2a$, $(x, y, z) \in [-a, a]^3$, and the exterior of the spheroid,

$$\frac{\xi_1^2}{r_a^2} + \frac{\xi_2^2 + \xi_3^2}{r_b^2} \geq 1, \quad \xi_1 = \frac{x + y + z}{\sqrt{3}}, \quad \xi_2 = \frac{x - z}{\sqrt{2}}, \quad \xi_3 = \frac{x - 2y + z}{\sqrt{6}}, \quad (5.11)$$

where the main axes of the spheroid are aligned with the orthonormal local coordinates ξ_i . The polar and equatorial radii of the spheroid are $r_a = a$, $r_b = \frac{a}{2}$. The reference length scale is equal to the half length of the cube edge, $L^* = a$.

The spheroid rotates around the semi-major axis ξ_1 with constant angular velocity $\vec{\omega}$,

$$\vec{\omega} = \omega \frac{\partial \vec{r}}{\partial \xi_1}, \quad (5.12)$$

such that the spheroid surface velocity \vec{v}^s at any point \vec{r} is tangent to the surface of the spheroid, that is

$$\vec{v}^s(\vec{r}) = \vec{\omega} \times \vec{r}. \quad (5.13)$$

The reference velocity is equal to the maximum velocity attained at the equator of the spheroid, $\xi_1 = 0$, and equal to $U^* = \omega r_b$.

The external magnetic field \vec{B}^0 is generated by a magnetic dipole with magnetic moment $\vec{m}(t)$, aligned with the semi-minor axis of the spheroid ξ_2 at $t = 0$, and rotating together with the spheroid. More precisely,

$$\vec{B}^0(\vec{r}, t) = \frac{\mu_0}{4\pi} \left(\frac{3\vec{r}(\vec{r} \cdot \vec{m})}{r^5} - \frac{\vec{m}}{r^3} \right), \quad \vec{m} = \vec{m}(t) = m_0 \left(\frac{\partial \vec{r}}{\partial \xi_2} \cos \omega t + \frac{\partial \vec{r}}{\partial \xi_3} \sin \omega t \right), \quad (5.14)$$

where m_0 is the strength of the magnetic dipole. The reference magnetic field magnitude is defined as the maximum magnitude of the magnetic field attained on the surface of the spheroid at $\vec{\xi}_\star = (0, r_b, 0)$, $t = 0$, and equal to $B^* = \|\vec{B}^0(\vec{\xi}_\star, 0)\| = \mu_0 m_0 / 2\pi r_b^3$.

The reference density and temperature are set to the initial uniform density and temperature, $\rho^* = \rho$, $T^* = T$ at $t = 0$. The properties of the plasma are constant and defined through the non-dimensional numbers $\text{Ma} = \text{M}_m = \text{Re} = \text{R}_m = \text{Pr} = 1$, $\gamma = 1.1$. The non-dimensional hyperbolic divergence cleaning speed is set to $c'_h = 1$. The non-dimensional initial conditions at $t = 0$ are set to $\rho' = T' = 1$, $\vec{v}' = 0$, $\vec{B}' = \vec{B}^0/B^*$, $\psi' = 0$. Boundary conditions include zero velocity on the cube surface and non-uniform velocity \vec{v}^s on the spheroid surface. All walls are assumed adiabatic, that is, $g(t) = 0$.

Two different cases are considered to cover our proposed magnetic boundary conditions. In the first case, the spheroid is electrically insulating, while the cube walls are electrically conducting with wall conductance parameter $c = 1$. In the second case, the spheroid surface is electrically conducting with $c = 1$, while the cube walls are electrically insulating. In both cases, the external magnetic field on all boundaries is \vec{B}^0 as defined in (5.14). Note that the two cases considered verify each of the discrete conditions (4.12) and (4.13) in general circumstances, including: curvilinear surface with non-zero velocity, non-homogeneous wall-normal magnetic field, not-steady state solution and boundary conditions, the velocity exhibits a large discontinuity on the spheroid surface at $t = 0$. We do not explicitly test for a perfectly conducting wall with $c = \infty$. This case corresponds to the homogeneous variant of (2.26) where the right-hand side is zero and is already covered by testing the magnetic boundary conditions with any positive value for wall conductance parameter, in particular, $c = 1$.

The computational domain is discretized with a curvilinear computational mesh with 1,474 tetrahedral elements; each split into four hexahedrons (see Figure 4). The mesh geometry and the solution are represented with polynomials of degree $p = 3$. Due to the nodal character of the entropy stability proofs of our boundary conditions, the polynomial degree p does not affect the entropy conservation properties. Therefore, the results for $p = 3$ we present here extend to any other values of p .

At the discrete level, the spheroid surface velocity \vec{v}^s is not exactly perpendicular to the (discrete) surface normal. Therefore, in order to satisfy condition (2.23), values of \vec{v}^s obtained from expression (5.13) cannot be used directly to specify the wall velocity \vec{v}^w in (4.12) and (4.13). Instead, the spheroid surface velocity values from (5.13) must be projected out of the discrete wall normal direction, that is

$$\vec{v}_j^w = \vec{v}_j^s - (\vec{v}_j^s \cdot \vec{n}_j) \vec{n}_j, \quad (5.15)$$

where the index j goes through all the nodes on the spheroid's surface, and \vec{n}_j is the unit normal at any such node.

Starting from the element-wise entropy conservation balance stated in (3.11), we turn off the interface dissipation mechanisms, $\text{DISS}^a = 0$ and $\text{DISS}^\nu = 0$, as well as the damping term in the divergence cleaning mechanism, $\alpha = 0$. Without these dissipation and damping terms, and after adding up the contributions of all the mesh elements, the total rate of change of discrete entropy exactly balances the discrete entropy production due to dissipation, that is

$$\frac{dS}{dt} + DT = 0, \quad \frac{dS}{dt} = \sum_k J_k \omega_k \frac{dS_k}{dt} = \sum_k J_k \omega_k \mathbf{w}_k^T \frac{d\mathbf{u}_k}{dt}, \quad DT = \sum_k J_k \omega_k \mathbf{g}_k^T C_k^\nu \mathbf{g}_k, \quad (5.16)$$

where index k goes through all nodes in the mesh and $\frac{d\mathbf{u}_k}{dt}$ corresponds to the time derivative in the left-hand side of (3.4).

The numerical verification of the entropy production balance (5.16) is shown in Figure 5. The time rate of change of the total discrete entropy, dS/dt , is always negative, while the entropy

production visco-resistive dissipation DT is always positive. Furthermore, dS/dt balances DT up to values close to machine epsilon for IEEE double precision floating point arithmetic.

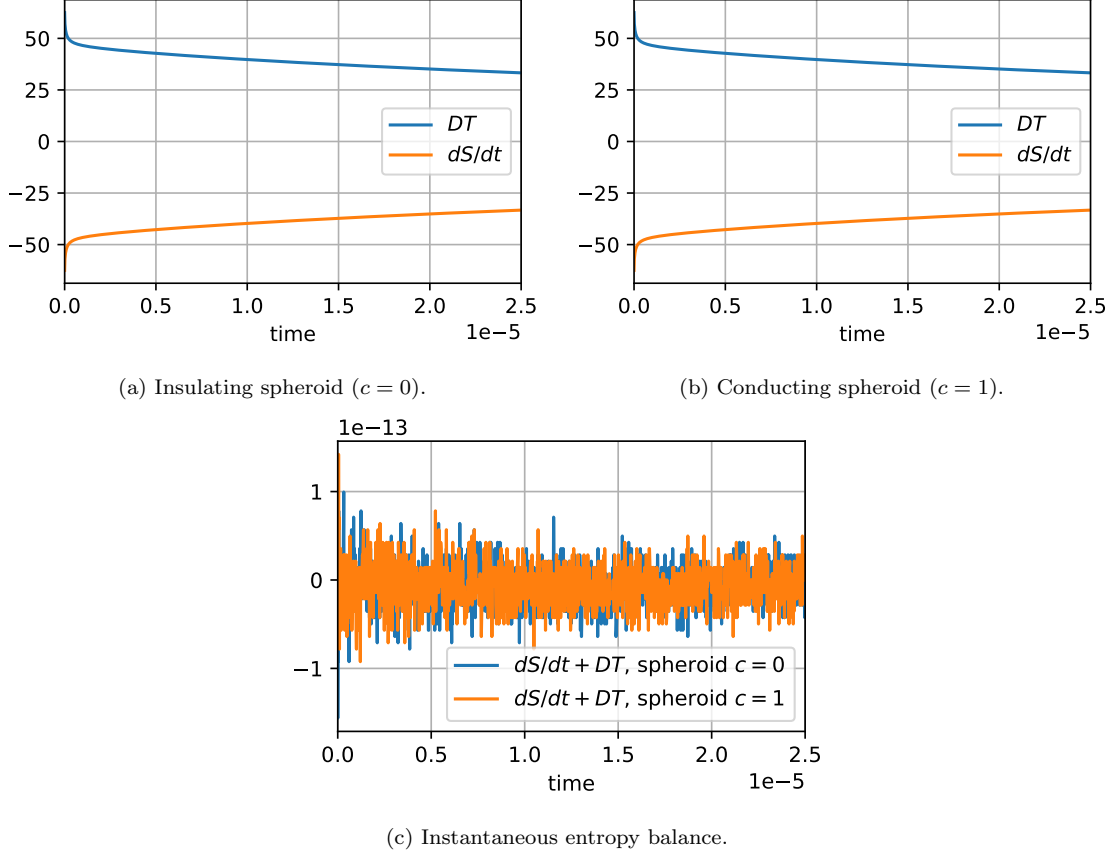


Figure 5: Discrete entropy conservation test: time derivative of the entropy function, dS/dt , dissipation term, DT , and instantaneous entropy production balance, $dS/dt + DT$, for electrically insulating ($c = 0$) and electrically conducting ($c = 1$) surface of the spheroid.

5.3. Fluid flow in microchannel

In this more practical example, we investigate a microfluidics application involving pumping and mixing in a microchannel. MHD techniques offer significant advantages for microfluidic applications, inducing bi-directional fluid motion without mechanical moving parts while requiring low voltage drops, which is compatible with biological samples and related applications. When an external magnetic field is applied to the fluid, a pass-through electric current generates a Lorentz force that drives the fluid motion.

A detailed description of the geometry used in this work can be found in [60] (Figure 3). For completeness, we also report a schematic of the setup; see Figure 6. The main channel is a cuboid with a rectangular base and a rectangular cross-section. The fluid comes in through symmetric side square channels at one end of the channel and goes out through the other end of the main channel. The channel features two sets of electrodes, denoted A-B and C-D. The voltage drop between electrodes A and B, located at side walls $y = \text{const.}$, and the accompanying electric current causes the fluid to flow along the channel (in x -direction) in an external magnetic field (in z -direction).

The voltage drop between another set of electrodes, *i.e.*, electrodes C and D, located on the bottom of the channel at $z = 0$, causes the fluid to circulate in loops parallel to the (x, y) -plane.

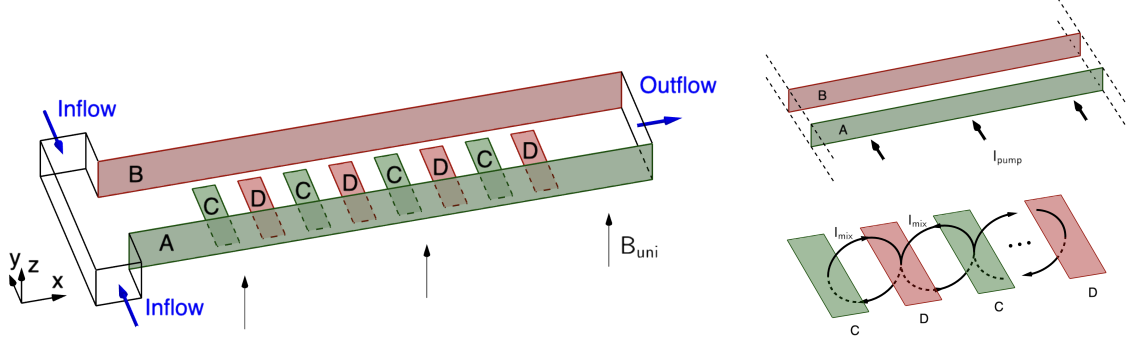


Figure 6: Microchannel flow test: schematic of the domain, uniform magnetic field \vec{B}_{uni} , and currents I_{pump} and I_{mix} .

The computational mesh includes 17,024 equal-sized cubic elements; the numerical solution is approximated with polynomials of degree $p = 5$ within each element. The solid wall boundaries of the channel are stationary ($\vec{v}^w = 0$) and adiabatic ($g(t) = 0$). Initial conditions are set to $\mathbf{v}_{init} = [\rho^0, \vec{0}, T^0, \vec{B}^0, 0]^T$, where ρ^0 , T^0 and \vec{B}^0 are the reference density, temperature, and external magnetic field, respectively.

At the inlet, we impose an uniform normal velocity, an external magnetic field \vec{B}^0 and zero normal gradients. The inlet velocity magnitude is defined such that the inlet mass flow rate at time step $n + 1$ equals the outlet mass flow rate at the previous time step n . The initial mass flow rate is zero. With the notation from Sections 4.1 and 4.2, the inlet manufacture state and gradients are defined as

$$\mathbf{v}_{(+)}^{inlet} = \left[\rho^0 \left(\frac{p_{(-)}}{p^0} \right)^{\frac{1}{\gamma}}, -V\vec{n}, T^0 \left(\frac{p_{(-)}}{p^0} \right)^{\frac{\gamma-1}{\gamma}}, \vec{B}^0, 0 \right]^T, \quad \theta_{(+)}^{inlet} = \theta_{(-)} - (\theta_{(-)} \cdot \vec{n}) \vec{n}, \quad (5.17)$$

where $V = \rho_{(+)}^{-1} A_{inlet}^{-1} \dot{m}$ is the inlet velocity directed against the outward normal vector \vec{n} , A_{inlet} is the total inlet area, and $\dot{m} = \int_{outlet} \rho(\vec{v} \cdot \vec{n}) da$ is the outlet mass flow rate at the previous time step. At the ghost inlet boundary node, the density $\rho_{(+)}$ and temperature $T_{(+)}$ are defined such that the pressure equals that of the internal state, that is $p_{(+)} = p_{(-)}$, and the specific entropy equals that of the reference state, that is $s_{(+)} = s^0(\rho^0, T^0)$.

At the outlet, we impose pressure, external magnetic field, and zero normal gradients,

$$\mathbf{v}_{(+)}^{outlet} = \left[\rho_{(-)} \left(\frac{p^0}{p_{(-)}} \right)^{\frac{1}{\gamma}}, \vec{v}_{(-)}, T_{(-)} \left(\frac{p^0}{p_{(-)}} \right)^{\frac{\gamma-1}{\gamma}}, \vec{B}^0, 0 \right]^T, \quad \theta_{(+)}^{outlet} = \theta_{(-)} - (\theta_{(-)} \cdot \vec{n}) \vec{n}, \quad (5.18)$$

where $p^0 = R\rho^0 T^0$ is the reference pressure. At the ghost outlet boundary node, the density $\rho_{(+)}$ and temperature $T_{(+)}$ are defined such that the pressure equals the reference pressure, that is $p_{(+)} = p^0$, and the specific entropy equals that of the internal state, that is $s_{(+)} = s_{(-)}$.

We encode electric currents passing through the conducting electrodes in the external magnetic field. The external magnetic field consists of three additive parts, $\vec{B}^0 = \vec{B}_{uni} + \vec{B}_{I_{pump}} + \vec{B}_{I_{mix}}$.

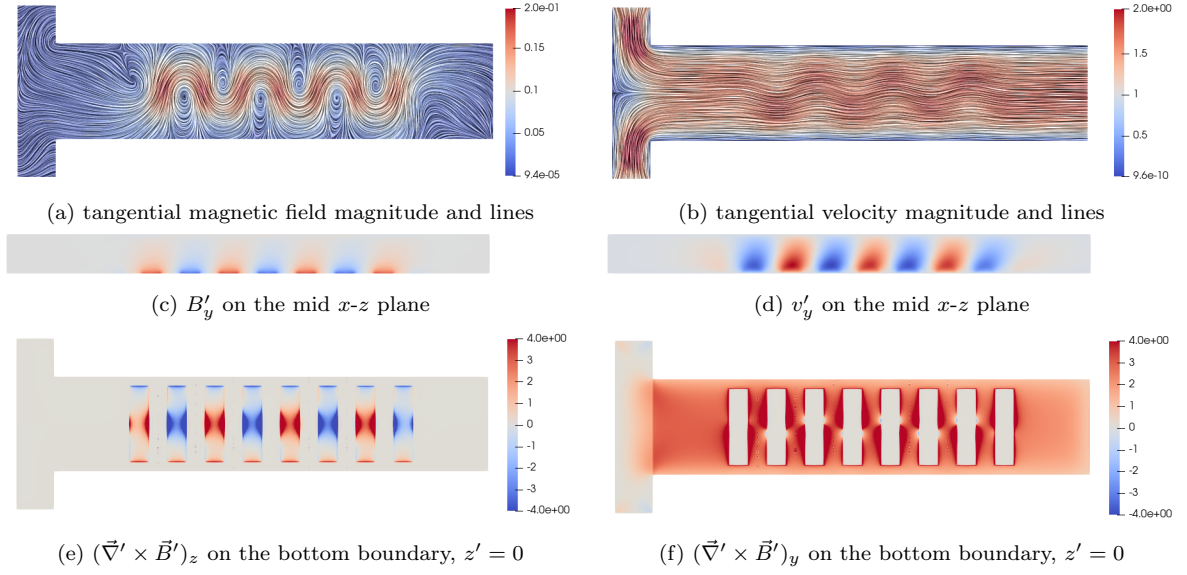


Figure 7: Microchannel flow: steady state solution on mid $x-y$ plane (a, b), mid $x-z$ plane (c, d), and bottom surface (e, f).

Here, $\vec{B}_{\text{uni}} = (0, 0, B_{\text{uni}})$ is a uniform background magnetic field directed along z -axis (see Figure 6). $\vec{B}_{I_{\text{pump}}}$ represents the magnetic field from a uniform electric current I_{pump} flowing in positive y -direction through an infinite straight conductor with rectangular cross-section, passing electrodes A and B, as shown in Figure 6. The analytical expression for $\vec{B}_{I_{\text{pump}}}$ can be found in [61] and in Appendix F. $\vec{B}_{I_{\text{mix}}}$ represents the magnetic field from a series of circular current loops I_{mix} , crossing neighboring electrodes in the direction from C to D within the fluid, as shown in Figure 6. The analytical expression for $\vec{B}_{I_{\text{mix}}}$ can be found in [62, 63] and in Appendix G. We assume patches A, B, C, and D to be perfectly electrically conducting, while other walls are perfectly electrically insulating.

Non-dimensional variables are defined through the thickness of the channel in the z -direction, $L^* = 0.2 \text{ mm}$ [60], the reference density and temperature, $\rho^* = \rho^0, T^* = T^0$, and the magnitude of the uniform external magnetic field, $B^* = B_{\text{uni}}$. The velocity scale U^* is approximately equal to the bulk velocity. The properties of the fluid are constant and defined such that $\text{Ma} = 0.01$ and $\text{Re} = 1.5$, which corresponds to a near-incompressible viscous flow. Because of incompressibility, the velocity and magnetic field do not significantly depend on the heat capacity ratio and thermal conductivity of the fluid, therefore we set $\gamma = 1.4$, $\text{Pr} = 0.72$. The magnetic Mach and Reynolds numbers are set to $\text{M}_m = 0.3$ and $\text{R}_m = 1.5$. The non-dimensional currents are $I'_{\text{pump}} = \mu_0 I_{\text{pump}} / B^* L^* = 0.72$, $I'_{\text{mix}} = \mu_0 I_{\text{mix}} / B^* L^* = 1$. The hyperbolic divergence cleaning speed is $c'_h = \text{Ma}^{-1}$.

After an initial transient period, the system reaches a steady state shown in Figure 7. We chose the problem parameters to quantitatively reproduce a sinusoidal flow pattern, as described in [60]. This sinusoidal flow pattern results from the combined effects of the pumping and mixing magnetic forces. According to the design of the boundary conditions, normal to the wall electric current is close to zero at the electrically insulating walls, as shown in Figure 7e where wall normal component of $\vec{\nabla} \times \vec{B}$, proportional to the electric current, is represented at the bottom boundary of the channel. At the conducting patches, normal electric current diverges from zero and concentrates near the

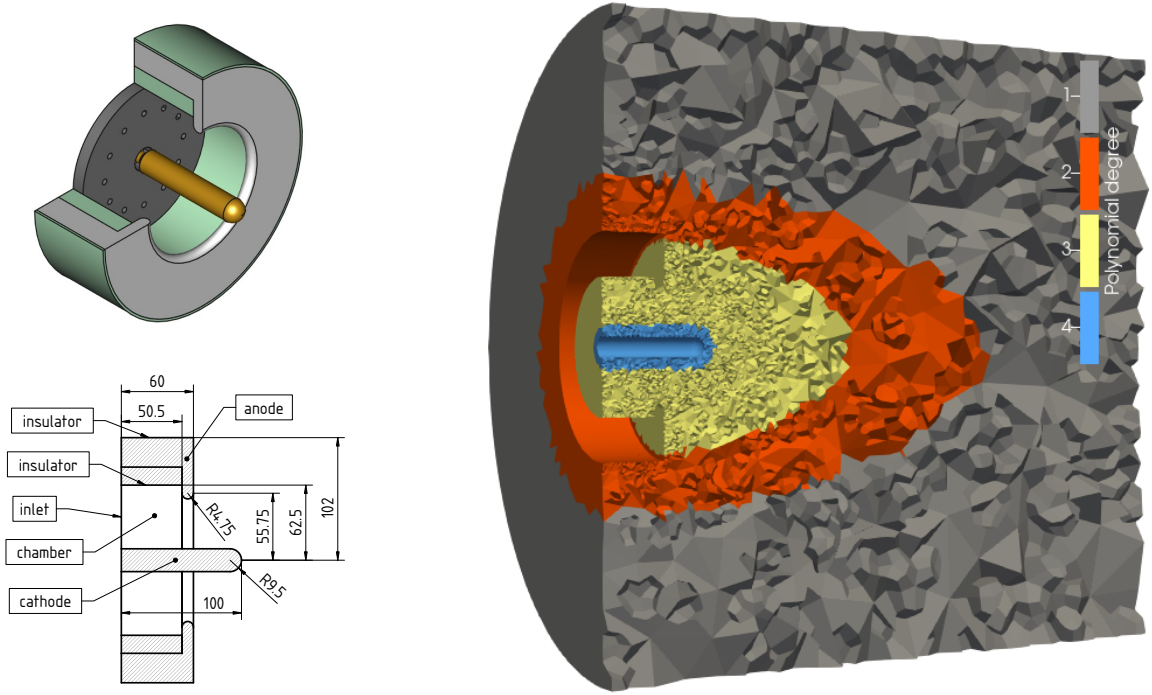


Figure 8: Princeton full-scale benchmark thruster: two-dimensional and three-dimensional schematics, computational domain, and grid. Sizes are given in mm. The solution is approximated with polynomials of varying degree from $p = 1$ to 4.

perimeter of the patches. The total electric current through the conducting patches corresponds to the value imposed through the external magnetic field \vec{B}^0 : it is positive for patches C and negative for patches D. The tangential electric current is close to zero at the perfectly conducting patches, as shown in Figure 7f where one of the tangential components of $\vec{\nabla} \times \vec{B}$ is represented at the same surface as in Figure 7e.

5.4. Self-field magnetoplasdynamic thruster

In this final test case, we focus on the compressible flow of ionized gas in a self-field magnetoplasdynamic (MPD) thruster, which is a type of electric propulsion device that utilizes the principles of magnetohydrodynamics (MHD) to generate thrust by accelerating an ionized gas. MPD thrusters are known for their compact design and efficiency, making them suitable for space applications. For our simulation, we chose the Princeton full-scale benchmark thruster (PFSBT), which has been extensively studied experimentally [64] and numerically [65, 66]. The geometry and specifications of the PFSBT are well-documented in the literature, including [64–66]. The thruster geometry features a cylindrical cathode and an annular anode, as shown in Figure 8. Argon is used as a propellant. The gas is injected in a chamber with insulating walls, partially through the 12 holes in the backplate and partially through a narrow channel at the base of the cathode. An electric arc ionizes the gas within a few millimeters downstream of the inlet. In its interaction with the self-induced magnetic field, the electric current flowing through the plasma accelerates the fluid by the Lorentz force.

Although our simulation does not aim to replicate the exact experimental regime, it provides

valuable insights into the fundamental behaviors of the thruster operation under simplified assumptions. Specifically, we assume an ideal gas model, constant viscosity, thermal conductivity, and electrical resistivity for the plasma. The operating conditions for the MPD thruster include temperatures exceeding 10^4 K, where internal molecular degrees of freedom become significant. In our model, we set the specific heat ratio $\gamma = 1.1$, as follows from [65] (Fig. 2). The argon gas constant is $R_{\text{Ar}} = 208.13 \text{ J kg}^{-1} \text{ K}^{-1}$.

Boundary conditions include zero velocity on the surface of the thruster and zero heat flux through it. The cathode and anode are perfectly electrically conducting, while the other parts of the thruster are perfectly electrically insulating. At the internal electrically insulating surface bounding the thruster chamber and also at the inlet, the external magnetic field is defined by the discharge current I_d flowing through the cathode. In cylindrical coordinates (r, θ, z) , the external magnetic field is

$$B_r^0 = B_z^0 = 0, \quad B_\theta^0 = \frac{I_d \mu_0}{4\pi r}, \quad \forall \vec{x} \in \Gamma^{\text{inlet}} \cup \Gamma^{\text{int-ins}}, \quad t > 0, \quad (5.19)$$

which is tangent to all the thruster surfaces. Thus, the normal magnetic field is zero at the conducting surfaces. At perfectly conducting surfaces, tangent components of the external magnetic field do not influence the solution and, therefore, can be set to zero. At the external insulating surface of the thruster, the external magnetic field can be assumed to be zero; the electric current flowing through the bulk of the anode approximately shields the magnetic field induced by currents in the cathode.

$$\vec{B}^0 = 0, \quad \forall \vec{x} \in \Gamma^{\text{cond}} \cup \Gamma^{\text{ext-ins}}, \quad t > 0. \quad (5.20)$$

In the simulation, the discharge current was set to $I_d = 5 \text{ kA}$ which is around 30 % of the operational discharge current equals 16 kA.

Following [65, 66], we further simplify the scheme of the propellant injection. The propellant is injected through the whole backplate of the chamber at a temperature high enough for the gas to be already ionized. The normal inlet velocity V is defined from the constant mass flux at the inlet resulting in a total mass flow rate of $\dot{m} = 6 \text{ g s}^{-1}$ – the operational mass flow rate of the thruster. In the notation of Section 4.1 and 4.2, the inlet boundary conditions are

$$\mathbf{v}_{(+)}^{\text{inlet}} = \left[\rho^0 \left(\frac{p_{(-)}}{p^0} \right)^{\frac{1}{\gamma}}, -V\vec{n}, T^0 \left(\frac{p_{(-)}}{p^0} \right)^{\frac{\gamma-1}{\gamma}}, \vec{B}^0, 0 \right]^T, \quad \theta_{(+)}^{\text{inlet}} = \theta_{(-)} - (\theta_{(-)} \cdot \vec{n})\vec{n}, \quad (5.21)$$

where the velocity $V = \rho_{(+)}^{-1} A_{\text{inlet}}^{-1} \dot{m}$ is directed against the outward-pointing normal vector \vec{n} and $A_{\text{inlet}} \approx 120 \text{ cm}^2$ is the inlet area. Density and temperature $\rho_{(+)}$ and $T_{(+)}$ are defined such that inlet pressure is that of the internal state, $p_{(+)} = p_{(-)}$, and specific entropy is that of the reference state, that is, $s_{(+)} = s^0(\rho^0, T^0)$. From a consideration of results from the previous simulations in [66], the reference density and temperature are set to $\rho^0 = 0.1 \text{ g m}^{-3}$, $T^0 = 10^5 \text{ K}$. The reference pressure $p^0 = R\rho^0 T^0$. The second expression in (5.21) amounts to imposing zero normal gradients for all variables. All other boundaries of the computational domain are treated as outlets.

The computational domain has a cylindrical shape with a diameter and length equal to six cathode lengths. It is large enough for the far-field outlet boundaries not noticeably to affect the solution, and such that all significant physical phenomena are captured within the region of interest close to the thruster. Outlet boundary conditions include zero magnetic field and external pressure

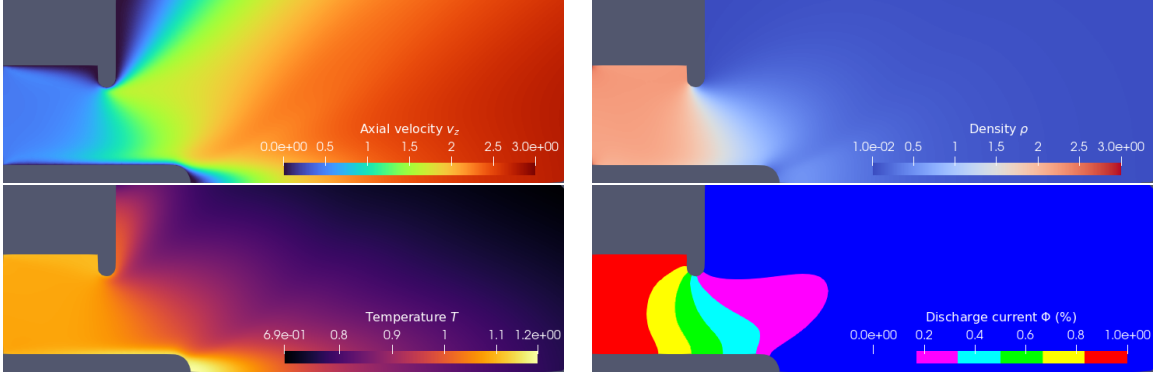


Figure 9: Princeton full-scale benchmark thruster: steady state solution for discharge current $I_d = 5$ kA.

$p^{\text{out}} = 10^{-2}p^0$ approximating a vacuum condition. In the notation of Section 4.1 and 4.2, outlet boundary conditions are

$$\mathbf{v}_{(+)}^{\text{out}} = \left[\rho_{(-)} \left(\frac{p^{\text{out}}}{p_{(-)}} \right)^{\frac{1}{\gamma}}, \vec{V}^{\text{out}}, T_{(-)} \left(\frac{p^{\text{out}}}{p_{(-)}} \right)^{\frac{\gamma-1}{\gamma}}, \vec{0}, 0 \right]^T, \quad \theta_{(+)}^{\text{inlet}} = \theta_{(-)} - (\theta_{(-)} \cdot \vec{n}) \vec{n}, \quad (5.22)$$

where $\vec{V}^{\text{out}} = \vec{v}_{(-)} - 2 \min(\vec{n} \cdot \vec{v}_{(-)}, 0) \vec{n}$ is the velocity of the gas with a simple limiter to prevent backflow if $\vec{n} \cdot \vec{v}_{(-)} < 0$. Density $\rho_{(+)}$ and temperature $T_{(+)}$ are defined such that the pressure $p_{(+)} = p^{\text{out}}$ and the specific entropy equals that of the internal state, that is $s_{(+)} = s_{(-)}$.

The problem is non-dimensionalized with the reference density and temperature, $\rho^* = \rho^0$, $T^* = T^0$, which are constant. Reference length $L^* = 0.1$ m equals the length of the cathode and approximately equal to the anode annular diameter. Reference velocity $V^* = \rho^{*-1} A_{\text{inlet}}^{-1} \dot{m} = 5 \text{ km s}^{-1}$ corresponds to the velocity of the gas at the inlet. The reference magnetic field magnitude $B^* = \mu_0 I_d / 2\pi r_c = 0.1$ T is the maximum magnitude of the magnetic field in the domain attained at the base of the cathode of radius $r_c = 0.95$ cm. Based on reference values, Mach number $\text{Ma} = 1$ and Alfvén Mach number $\text{M}_m = 0.5$. Viscosity, electrical resistivity, and thermal conductivity are defined such that $\text{Re} = 500$, $\text{R}_m = 50$, and $\text{Pr} = 2/3$. The magnetic Reynolds number $\text{R}_m = 50$ is chosen to prevent convection of the magnetic field lines outside of the thruster chamber to qualitatively reproduce [65, 66]. Hyperbolic divergence cleaning speed $c'_h = \text{M}_m^{-1}$.

The unstructured computational mesh consists of 113,643 tetrahedral elements, each subdivided into four equally sized hexahedral elements, as shown in Figure 8. The mesh is refined in the region of interest so that the maximum edge length of the tetrahedral elements near the cathode is $r_c/2$, while in the far-field zone, it grows progressively up to $5r_c$. An approximately steady-state solution was obtained using polynomials degrees gradually varying from $p = 1$ in the under-resolved far-field region and up to $p = 4$ in the region close to the cathode boundary. The polynomial degree used in the different regions is indicated with varying colors in Figure 8. An entropy-stable algorithm with h/p-nonconforming refinement was used, following the formulation from [23]. To handle the pressure drop to a near-vacuum condition, the density was artificially constrained to not drop below $10^{-2}\rho^*$. This limiter is active in the under-resolved far-field region, away from the area of interest. The solution preserves axisymmetry, including $v_\theta = 0$ and $B_z = B_r = 0$. The dimensionless divergence of the magnetic field in the L_2 norm remains under $\|\nabla' \cdot \vec{B}'\|_2 < 10^{-2}$.

First, the simulation remains stable at all time. Second, in agreement with experimental observations and previous simulations, the plasma accelerates significantly as it passes through

the thruster chamber, as shown in Figure 9. A significant part of the total thrust can be referred to the high pressure at the exit from the thruster chamber. From a comparison with a numerical solution of the compressible Navier–Stokes equations under the same hydrodynamic conditions, the electromagnetic contribution to the thrust is estimated to be 10 % of the total thrust. This relatively low fraction correlates with the weak discharge current we chose for this simulation, and consistent with an extrapolation of the discharge current vs. electromagnetic thrust trend presented in [65] (Table 1).

Due to the axial symmetry of the solution, the electric current has a stream function $\Phi = rB_\theta$ shown in Figure 9. Electric current streamlines lie on iso-surfaces of Φ . Consistently with the continuous analysis, all the electric current streamlines originate at the cathode surface and end at the anode surface. The gas tends to convect electric current streamlines downstream of the thruster chamber, while the electrical resistivity keeps such spread within the nearby region.

6. Conclusions

We have used entropy stability and the summation-by-parts framework to derive entropy conservative and entropy stable wall boundary conditions for the resistive magnetohydrodynamic equations in the presence of an adiabatic wall or a wall with a prescribed heat entropy flow, addressing three scenarios: electrically insulating walls, thin walls with finite conductivity, and perfectly conducting walls. A point-wise entropy-stable numerical procedure has been presented for weakly enforcing these solid wall boundary conditions at the semi-discrete level, combining a penalty flux approach with a simultaneous approximation-term technique. The resulting semi-discrete operator mimics exactly the behavior at the continuous level, and the proposed non-linear boundary treatment provides a mechanism for ensuring non-linear stability in the L_2 norm of the continuous and semi-discretized resistive magnetohydrodynamic equations.

The design order properties of the scheme are validated in the context of laminar flow of an electrically conducting fluid in a circular pipe, under an external transverse uniform magnetic field and an external uniform force in the axial direction driving the fluid movement. The entropy conservation properties of the proposed numerical technique have been assessed through a numerical experiment involving the flow around a stationary rotating spheroid. The error in the entropy function balance showed an excellent agreement with the theory for a mix of electrically insulating and electrically conducting walls. The pumping and mixing of conducting fluid in a microchannel have been showcased as an application to microfluidics. The numerical results show very good agreement with the results available from the literature.

The robustness of the complete semi-discrete operator (*i.e.*, the entropy-stable interior operator coupled with the new boundary treatment) has been demonstrated for a self-field magnetoplasma-dynamic thruster with a considerable pressure drop. The numerical simulation has been performed with a p -refinement approach, leading to a numerical solution that shows excellent agreement with the results available from the literature. This test has been successfully computed without the need to introduce artificial dissipation or filtering to stabilize the computations. Although the robustness and efficacy of the techniques presented in this work have been validated using discontinuous spectral collocation operators on unstructured grids, the new boundary conditions can be applied to a comprehensive class of spatial discretizations. They are compatible with any diagonal-norm summation-by-parts spatial operator, including finite element, finite difference, finite volume, nodal and modal discontinuous Galerkin, and flux reconstruction schemes.

Acknowledgements

The research reported in this paper was funded by King Abdullah University of Science and Technology. We are thankful for the computing resources of the Supercomputing Laboratory at King Abdullah University of Science and Technology and, in particular, Shaheen III supercomputer.

Appendix A. Entropy stable two-point flux function

The entropy consistent two point flux function for the discrete GLM-MHD system (3.4) derived in [19] is

$$\mathbf{f}_{(i,j)}^{\text{EC}} = \begin{pmatrix} f_1^{\text{EC}} \\ \vdots \\ f_5^{\text{EC}} \\ \vdots \\ f_9^{\text{EC}} \end{pmatrix} = \begin{pmatrix} \rho^{\ln} \{v_1\} \\ \rho^{\ln} \{v_1\}^2 + \bar{p} + \frac{1}{2\mu_0} \left(\{B_1^2\} + \{B_2^2\} + \{B_3^2\} \right) - \frac{1}{\mu_0} \{B_1\}^2 \\ \rho^{\ln} \{v_1\} \{v_2\} - \frac{1}{\mu_0} \{B_1\} \{B_2\} \\ \rho^{\ln} \{v_1\} \{v_3\} - \frac{1}{\mu_0} \{B_1\} \{B_3\} \\ f_5^{\text{EC}} \\ c_h \{\psi\} \\ \{v_1\} \{B_2\} - \{v_2\} \{B_1\} \\ \{v_1\} \{B_3\} - \{v_3\} \{B_1\} \\ c_h \{B_1\} \end{pmatrix}, \quad (\text{A.1})$$

where

$$\begin{aligned} f_5^{\text{EC}} = & f_1^{\text{EC}} \left[\frac{1}{(\gamma - 1)\beta^{\ln}} - \frac{1}{2} \left(\{v_1^2\} + \{v_2^2\} + \{v_3^2\} \right) \right] + f_2^{\text{EC}} \{v_1\} + f_3^{\text{EC}} \{v_2\} + f_4^{\text{EC}} \{v_3\} \\ & + \frac{1}{\mu_0} \left[f_6^{\text{EC}} \{B_1\} + f_7^{\text{EC}} \{B_2\} + f_8^{\text{EC}} \{B_3\} - \frac{1}{2} \left(\{v_1 B_1^2\} + \{v_1 B_2^2\} + \{v_1 B_3^2\} \right) \right. \\ & \left. + \{v_1 B_1\} \{B_1\} + \{v_2 B_2\} \{B_1\} + \{v_3 B_3\} \{B_1\} + f_9^{\text{EC}} \{\psi\} - c_h \{B_1 \psi\} \right] \end{aligned}$$

and

$$\bar{p} = \frac{\{\rho\}}{\{\beta\}}, \quad \beta = \frac{\rho}{p}.$$

The previous expressions use of the arithmetic and logarithmic means, respectively, defined as follow,

$$\{a\} := \frac{1}{2}(a_i + a_j), \quad a^{\ln} := \frac{a_j - a_i}{\ln a_j - \ln a_i}.$$

Appendix B. Jacobian of the transformation from entropy to conservative variables

The Jacobian of the transformation matrix from conservative variables, \mathbf{u} , to entropy variables \mathbf{w} , for GLM-MHD system, *i.e.*, $\mathcal{H} = \partial \mathbf{u} / \partial \mathbf{w}$ is defined in [19]. In the following, we reproduce its expression. Our definition has an additional $1/R$ scaling factor related to our choice of entropy function, S , in (2.14) and (2.15).

Consider a state of the GLM-MHD system defined in primitive variables as $\mathbf{v} = (\rho, v_1, v_2, v_3, T, B_1, B_2, B_3, \psi)$. Then,

$$\mathcal{H} = \frac{1}{R} \begin{bmatrix} \rho & \rho v_1 & \rho v_2 & \rho v_3 & \mathcal{E} & 0 & 0 & 0 & 0 \\ \rho v_1 & \rho v_1^2 + p & \rho v_1 v_2 & \rho v_1 v_3 & (\mathcal{E} + p)v_1 & 0 & 0 & 0 & 0 \\ \rho v_2 & \rho v_2 v_1 & \rho v_2^2 + p & \rho v_2 v_3 & (\mathcal{E} + p)v_2 & 0 & 0 & 0 & 0 \\ \rho v_3 & \rho v_3 v_1 & \rho v_3 v_2 & \rho v_3^2 + p & (\mathcal{E} + p)v_3 & 0 & 0 & 0 & 0 \\ \mathcal{E} & (\mathcal{E} + p)v_1 & (\mathcal{E} + p)v_2 & (\mathcal{E} + p)v_3 & \mathcal{H}_{5,5} & \tau B_1 & \tau B_2 & \tau B_3 & \tau \psi \\ 0 & 0 & 0 & 0 & \tau B_1 & \tau \mu_0 & 0 & 0 & 0 \\ 0 & 0 & 0 & 0 & \tau B_2 & 0 & \tau \mu_0 & 0 & 0 \\ 0 & 0 & 0 & 0 & \tau B_3 & 0 & 0 & \tau \mu_0 & 0 \\ 0 & 0 & 0 & 0 & \tau \psi & 0 & 0 & 0 & \tau \mu_0 \end{bmatrix}, \quad (\text{B.1})$$

$$\tau = \frac{p}{\rho} = RT \quad (\text{B.2})$$

$$\mathcal{E} = \frac{p}{\gamma - 1} + \rho \frac{\|\vec{v}\|^2}{2}, \quad (\text{B.3})$$

$$\mathcal{H}_{5,5} = \frac{1}{\rho} \left(\frac{p^2}{\gamma - 1} + \mathcal{E}^2 \right) + p \|\vec{v}\|^2 + \frac{\tau}{\mu_0} \left(\|\vec{B}\|^2 + \psi^2 \right). \quad (\text{B.4})$$

Appendix C. Motivation for the discrete boundary condition for electrically conducting walls

According to the expression for the diffusive flux (2.9), the magnetic boundary conditions for electrically conducting walls (2.26) define the normal resistive flux at the boundary, that is

$$\hat{\mathbf{f}}_{(\vec{B})}^{\nu} \cdot \vec{n} = \frac{\mu_R}{\mu_0} \left(\vec{\nabla} \vec{B} - \vec{\nabla} \vec{B}^T \right) \cdot \vec{n} \equiv \frac{\mu_R}{\mu_0} \left[(\vec{\nabla} \times \vec{B}) \times \vec{n} \right]^T = \frac{\mu_R}{\mu_0} c_d^{-1} \left(\vec{B}_t^0 - \vec{B}_t \right)^T, \quad \vec{x} \in \Gamma^{\text{cond}}, \quad t > 0, \quad (\text{C.1})$$

where \vec{B}_t^0 and \vec{B}_t denote the tangential components of the corresponding vectors. Note that the right hand side of (C.1) is expressed here explicitly in terms of tangent components of the magnetic field; this form is equivalent to the conditions in (2.26) due to the continuity of the normal component of the magnetic field across the boundary.

The discrete boundary conditions (4.13) were designed to mimic (C.1) on a discrete level. The numerical resistive flux $\hat{\mathbf{f}}_{(\vec{B})}^{\nu}(\mathbf{u}_{(-)}, \mathbf{u}_{(+)})$ defined in (3.9) is a linear function of the gradients, therefore it can be expressed as

$$\hat{\mathbf{f}}_{(\vec{B})}^{\nu}(\mathbf{u}_{(-)}, \mathbf{u}_{(+)}) = \frac{\mu_R}{\mu_0} \left(\hat{\theta}_{(\vec{B})} - \hat{\theta}_{(\vec{B})}^T \right), \quad \hat{\theta}_{(\vec{B})} = \frac{1}{2} \left(\theta_{(\vec{B})}^{(-)} + \theta_{(\vec{B})}^{(+)} \right), \quad (\text{C.2})$$

where $\hat{\theta}_{(\vec{B})}$ is a numerical magnetic boundary gradient. Direct substitution of the boundary gradients from (4.13) into the expression for the numerical boundary gradient $\hat{\theta}_{(\vec{B})}$ in (C.2) results in

$$\hat{\theta}_{(\vec{B})} = \frac{1}{2} \left(\theta_{(\vec{B})} + \theta_{(\vec{B})}^T \right)^{(-)} + c_d^{-1} \left(\vec{B}^0 - \vec{B} \right)^T \vec{n}. \quad (\text{C.3})$$

As the resistive flux depends on the antisymmetric part of the gradients, only the second term of (C.3) contributes to the normal numerical resistive flux at the boundary, which therefore simplifies

to

$$\hat{\mathbf{f}}_{(\vec{B})}^{\nu}(\mathbf{u}_{(-)}, \mathbf{u}_{(+)}) \cdot \vec{n} = \frac{\mu_R}{\mu_0} c_d^{-1} \left((\vec{B}^0 - \vec{B})^T \vec{n} - \vec{n}^T (\vec{B}^0 - \vec{B}) \right) \cdot \vec{n} = \frac{\mu_R}{\mu_0} c_d^{-1} (\vec{B}_t^0 - \vec{B}_t)^T. \quad (\text{C.4})$$

The discrete expression (C.4) mimics the continuous expression (C.1) and substantiates the particular form of the boundary gradient (4.13) for electrically conducting walls. In particular, for the case of perfectly conducting boundary ($c_d^{-1} = 0$), the numerical resistive flux through the boundary is identically zero.

Appendix D. Analytical solution for MHD pipe flow

In this section, we present an analytical solution to the flow of a conducting fluid in a straight pipe of circular cross-section under uniform traverse magnetic field. This analytical solution is derived in [59] and used in section 5.1 to validate the accuracy of the solid wall boundary conditions we propose in this work. An uniform external force in the axial direction causes the fluid motion, and the flow is assumed incompressible.

Within the pipe, the solution satisfies the incompressible visco-resistive MHD equations,

$$\begin{aligned} \rho(\vec{v} \cdot \vec{\nabla})\vec{v} &= -\nabla \vec{p} + \eta \vec{\nabla}^2 \vec{v} + \frac{1}{\mu_0} (\vec{\nabla} \times \vec{B}) \times \vec{B} + F, \quad \vec{\nabla} \cdot \vec{v} = 0, \\ \sigma \mu_0 \vec{\nabla} \times (\vec{v} \times \vec{B}) - \vec{\nabla} \times (\vec{\nabla} \times \vec{B}) &= 0, \quad \vec{\nabla} \cdot \vec{B} = 0, \end{aligned} \quad (\text{D.1})$$

where the density ρ , viscosity η , and conductivity σ of the fluid are constant, and F is an external force.

We set a Cartesian coordinate system such that the x -axis is parallel to the uniform traverse external magnetic field of strength B^0 , and the z -axis coincides with the longitudinal axis of the pipe of radius a . Assuming laminar flow, the velocity and magnetic field of the solution take the form

$$\vec{v} = (0, 0, u), \quad \vec{B} = (B^0, 0, b), \quad (\text{D.2})$$

where functions $u = u(r, \theta)$ and $b = b(r, \theta)$ are defined in the cross-section in non-dimensional polar coordinates $r = a^{-1} \sqrt{x^2 + y^2}$ and θ , and satisfies the following boundary conditions,

$$u = 0, \quad b + c \frac{\partial b}{\partial r} = 0, \quad \text{at } r = 1, \quad (\text{D.3})$$

where $c = \tau_w \sigma_0 / a \sigma$ is a dimensionless wall conductance parameter depending on the thickness of the wall τ_w and conductivity of the wall material σ_0 . For electrically insulating walls ($c = 0$), the boundary condition for b (D.3) reduces to the Dirichlet condition $b|_{r=1} = 0$. For perfectly conducting wall ($c = \infty$), (D.3) reduces to the Neumann condition $\partial_r b|_{r=1} = 0$.

The second governing dimensionless parameter is the Hartmann number $\text{Ha} = a B^0 \sqrt{\sigma / \eta}$, expressing the ratio of electromagnetic force to the viscous force. With the auxiliary constant $k = \text{Ha} / 2$, the solution is given as a truncated series of the form

$$\begin{aligned} \frac{\eta}{a^2 F} u(r, \theta) &= \tilde{u}(r, \theta) = - \sum_{n=0}^{N_0} \frac{\epsilon_n}{k} M_n \frac{(-1)^n e^{kr \cos \theta} + e^{-kr \cos \theta}}{2} I_n(kr) \cos(n\theta), \\ \frac{\sqrt{\eta}}{a^2 F \mu_0 \sqrt{\sigma}} b(r, \theta) &= \tilde{b}(r, \theta) = + \sum_{n=0}^{N_0} \frac{\epsilon_n}{k} M_n \frac{(-1)^n e^{kr \cos \theta} - e^{-kr \cos \theta}}{2} I_n(kr) \cos(n\theta) - \frac{r}{2k} \cos(\theta), \end{aligned} \quad (\text{D.4})$$

where $I_n(k)$ are modified Bessel functions of the first kind. The coefficients ϵ_n and M_n are defined as

$$\begin{aligned}\epsilon_n &= \begin{cases} 1/2, & \text{if } n = 0, \\ 1, & \text{otherwise,} \end{cases} \\ M_n &= \sum_{s=0}^{S_0} A_s \frac{I_{n+2s+1}(k) + I_{n-2s-1}(k)}{I_n(k)}.\end{aligned}\tag{D.5}$$

Bessel functions of negative order can be computed based on their symmetry, $I_n = I_{-n}$. The coefficients A_s are computed from the solution of the linear system of equations $B_{ms}A_s = C_m$, $0 \leq s, m \leq S_1$, where $S_1 \leq S_0$. For finite values of c , we have

$$\begin{aligned}B_{ms} &= \delta_{ms} + ck \sum_{n=0}^{N_1} (-1)^{n+1} \frac{\epsilon_n I'_n(k)}{I_n(k)} [I_{n+2s+1}(k) + I_{n-2s-1}(k)] [I_{n+2m+1}(k) + I_{n-2m-1}(k)], \\ C_m &= \begin{cases} -\frac{1+c}{2}, & \text{if } m = 0, \\ 0, & \text{otherwise,} \end{cases}\end{aligned}\tag{D.6}$$

where $I'_n(k)$ is a derivative of the Bessel function, computed as

$$I'_n(k) = \frac{I_{n-1}(k) + I_{n+1}(k)}{2}.\tag{D.7}$$

In case of large values of c , or even in the extreme $c = \infty$, the entries of the matrix B_{ms} and the right hand side C_m should be divided by c to get alternative expressions with better numerical conditioning and thus more amenable to computation.

The analytical solution is expressed in non-dimensional variables as defined in (5.1)–(5.7). The reference quantities are defined such that the non-zero components of the solution (ρ' , T' , v'_z , B'_x , B'_z) have maximum magnitudes of order one. To this end, the reference length is defined as the pipe radius, that is $L^* = a$. Due to incompressibility and temperature fluctuations damping mechanism, described in section 5.1, density and temperature are constant and arbitrary, therefore the reference density and temperature can be set as $\rho^* = \rho$ and $T^* = T$ respectively. The reference magnetic field magnitude is set to that of the external magnetic field, that is, $B^* = B^0$. The reference velocity is set to the velocity at the center line, that is $U^* = u(0, 0)$. The other reference quantities are defined through dimensionless numbers. The dimensionless external force F' and the magnetic Mach and Reynolds numbers M_m and R_m are chosen such that the solution satisfies $u(0, 0) = b(\frac{1}{2}, \pi) = 1$ ³. To that end, we set

$$F' = \frac{1}{\text{Re } \tilde{u}_\star}, \quad M_m = \sqrt{\frac{\text{Re } \tilde{u}_\star}{\text{Ha } \tilde{b}_\star}}, \quad R_m = \text{Ha } \frac{\tilde{u}_\star}{\tilde{b}_\star}.\tag{D.8}$$

where $\tilde{u}_\star = \tilde{u}(0, 0)$ and $\tilde{b}_\star = \tilde{b}(\frac{1}{2}, \pi)$. As the solution corresponds to an incompressible flow regime, the Prandtl number and the heat capacity ratio are chosen arbitrarily and set to $\gamma = \frac{7}{5}$ and $\text{Pr} = \frac{3}{4}$. With all the previous definition, the non-dimensional solution takes the following final form

$$\rho' = 1, \quad \vec{v}' = (0, 0, \tilde{u}_\star^{-1} \tilde{u}), \quad T' = 1, \quad \vec{B}' = (1, 0, \tilde{b}_\star^{-1} \tilde{b}).\tag{D.9}$$

³At the coordinate $(r, \theta) = (\frac{1}{2}, \pi)$ the axial magnetic field is close to its maximum value for all values of c .

The finite summation limits N_0, S_0, N_1 , and S_1 in (D.4)–(D.6) truncate the infinite series. These summation limits should be set to large enough values to achieve the required accuracy. In practice, we set $N_0 = N_1 = 30$ and $S_0 = S_1 = 10$. At $\text{Ha} = 5$, and for all the values of c we tested, these summation limit values provide a maximum relative error less than 10^{-15} , which is close to machine epsilon for IEEE double precision floating point arithmetic.

Appendix E. Raw data from convergence study

Table E.1 reproduces the raw data of the convergence study presented in Section 5.1.

Appendix F. Magnetic field of a wire with rectangular cross-section

Here, we reproduce an analytical expression for the magnetic field induced by an uniform electric current flowing through a conducting medium of infinite length with rectangular cross section of width w and thickness h [61]. This analytical solution can be used to approximate the solution of a finite domain of length L with $w \ll L$ and $h \ll L$. In Cartesian coordinates, with the current of density i flowing in positive y direction through the wire of rectangular cross section $(x, z) \in [-w/2, w/2] \times [-h, 0]$, the components of the induced magnetic field \vec{B} are

$$\begin{aligned} B_x &= \tilde{B}_x\left(x + \frac{w}{2}, z\right) - \tilde{B}_x\left(x - \frac{w}{2}, z\right), \\ B_y &= 0, \\ B_z &= \tilde{B}_z\left(x + \frac{w}{2}, z\right) - \tilde{B}_z\left(x - \frac{w}{2}, z\right), \end{aligned}$$

where

$$\begin{aligned} \tilde{B}_x(p, z) &= \frac{\mu_0 i}{4\pi} \left[p \ln \left(1 + \frac{h^2 + 2zh}{p^2 + z^2} \right) + 2(z + h) \arctan \left(\frac{p}{z + h} \right) - 2z \arctan \left(\frac{p}{z} \right) \right], \\ \tilde{B}_z(p, z) &= \frac{\mu_0 i}{4\pi} \left[z \ln \left(1 + \frac{p^2}{z^2} \right) - (z + h) \ln \left(1 + \frac{p^2}{(z + h)^2} \right) - 2p \left(\arctan \left(\frac{z + h}{p} \right) - \arctan \left(\frac{z}{p} \right) \right) \right]. \end{aligned}$$

Appendix G. Magnetic field of a circular current loop

Here, we reproduce the expressions for the magnetic field induced by a closed circular current loop [62, 63]. In cylindrical coordinates (r, θ, z) , a total current I flows through the circular loop with coordinates $z = 0, r = a$ in the direction of incrementing θ . For any point in space that is not on the current loop, the components of the magnetic field are

$$\begin{aligned} B_r &= B_0 \frac{\gamma}{\pi \sqrt{Q}} \left(E(k) \frac{1 + \alpha^2 + \beta^2}{Q - 4\alpha} - K(k) \right), \quad B_\theta = 0, \\ B_z &= B_0 \frac{1}{\pi \sqrt{Q}} \left(E(k) \frac{1 - \alpha^2 - \beta^2}{Q - 4\alpha} + K(k) \right), \end{aligned}$$

where

$$\alpha = \frac{r}{a}, \quad \beta = \frac{z}{a}, \quad \gamma = \frac{z}{r}, \quad Q = (1 + \alpha)^2 + \beta^2, \quad k = \sqrt{\frac{4\alpha}{Q}}, \quad B_0 = \frac{I\mu_0}{2a},$$

and $K(k)$ and $E(k)$ are the complete elliptic integral functions of the first and second kind, respectively.

References

- [1] Godunov, S. K., “Symmetric form of the equations of magnetohydrodynamics,” *Numerical Methods for Mechanics of Continuum Medium*, Vol. 1, 1972, pp. 26–34.
- [2] Davidson, P. A. and Thess, A., *Magnetohydrodynamics*, Vol. 418, Springer Science & Business Media, 2002.
- [3] Davidson, P. A., *An Introduction to Magnetohydrodynamics*, Cambridge Texts in Applied Mathematics, Cambridge University Press, 2001.
- [4] Hosking, R. J., Dewar, R. L., et al., *Fundamental fluid mechanics and magnetohydrodynamics*, Springer, 2016.
- [5] Harms, A. A., Kingdon, D. R., Miley, G. H., and Schoepf, K. F., *Principles of fusion energy: an introduction to fusion energy for students of science and engineering*, World Scientific Publishing Company, 2000.
- [6] Marcus, F. B., *Systems Approaches to Nuclear Fusion Reactors*, Springer, 2022.
- [7] Powell, K. G., Roe, P. L., Linde, T. J., Gombosi, T. I., and De Zeeuw, D. L., “A solution-adaptive upwind scheme for ideal magnetohydrodynamics,” *Journal of Computational Physics*, Vol. 154, No. 2, 1999, pp. 284–309.
- [8] Dafermos, C. M., *Hyperbolic Conservation Laws in Continuum Physics*, Springer, 4th ed., 2016.
- [9] Fischer, P., Min, M., Rathnayake, T., Dutta, S., Kolev, T., Dobrev, V., Camier, J.-S., Kronbichler, M., Warburton, T., Świrzydowicz, K., et al., “Scalability of high-performance PDE solvers,” *The International Journal of High Performance Computing Applications*, Vol. 34, No. 5, 2020, pp. 562–586.
- [10] Isaac, T. and Knepley, M. G., “Support for non-conformal meshes in PETSc’s DMplex interface,” *arXiv preprint arXiv:1508.02470*, 2015.
- [11] Rojas, D., Boukhafane, R., Dalcin, L., Del Rey Fernández, D. C., Ranocha, H., Keyes, D. E., and Parsani, M., “On the robustness and performance of entropy stable collocated discontinuous Galerkin methods,” *Journal of Computational Physics*, Vol. 426, 2021, pp. 109891.
- [12] Hesthaven, J. S., *Numerical methods for conservation laws: From analysis to algorithms*, SIAM, 2017.
- [13] Wang, Z. J., Fidkowski, K., Abgrall, R., Bassi, F., Caraeni, D., Cary, A., Deconinck, H., Hartmann, R., Hillewaert, K., Huynh, H. T., et al., “High-order CFD methods: current status and perspective,” *International Journal for Numerical Methods in Fluids*, Vol. 72, No. 8, 2013, pp. 811–845.
- [14] Reyna Nolasco, I. E., Er-Raiy, A., Boukhafane, R., Aldhfeeri, A. A., Dalcin, L., and Parsani, M., “Eigenanalysis and non-modal analysis of collocated discontinuous Galerkin discretizations with the summation-by-parts property,” *Computers & Mathematics with Applications*, Vol. 124, 2022, pp. 196–217.
- [15] Fisher, T. C. and Carpenter, M. H., “High-order entropy stable finite difference schemes for nonlinear conservation laws: Finite domains,” *Journal of Computational Physics*, Vol. 252, 2013, pp. 518–557.
- [16] Carpenter, M. H., Fisher, T. C., Nielsen, E. J., and Frankel, S. H., “Entropy stable spectral collocation schemes for the Navier–Stokes equations: Discontinuous interfaces,” *SIAM Journal on Scientific Computing*, Vol. 36, No. 5, 2014, pp. B835–B867.
- [17] Bohm, M., Winters, A. R., Gassner, G. J., Derigs, D., Hindenlang, F., and Saur, J., “An entropy stable nodal discontinuous Galerkin method for the resistive MHD equations. Part I: Theory and numerical verification,” *Journal of Computational Physics*, Vol. 422, 2020, pp. 108076.
- [18] Rueda-Ramírez, A. M., Hennemann, S., Hindenlang, F. J., Winters, A. R., and Gassner, G. J., “An entropy stable nodal discontinuous Galerkin method for the resistive MHD equations. Part II: Subcell finite volume shock capturing,” *Journal of Computational Physics*, Vol. 444, 2021, pp. 110580.
- [19] Derigs, D., Winters, A. R., Gassner, G. J., Walch, S., and Bohm, M., “Ideal GLM-MHD: About the entropy consistent nine-wave magnetic field divergence diminishing ideal magnetohydrodynamics equations,” *Journal of Computational Physics*, Vol. 364, 2018, pp. 420–467.
- [20] Dalcin, L., Rojas, D., Zampini, S., Fernández, D. C. D. R., Carpenter, M. H., and Parsani, M., “Conservative and entropy stable solid wall boundary conditions for the compressible Navier–Stokes equations: Adiabatic wall and heat entropy transfer,” *Journal of Computational Physics*, Vol. 397, 2019, pp. 108775.
- [21] Parsani, M., Carpenter, M. H., and Nielsen, E. J., “Entropy stable wall boundary conditions for the three-dimensional compressible Navier–Stokes equations,” *Journal of Computational Physics*, Vol. 292, 2015, pp. 88–113.
- [22] Carpenter, M. H., Parsani, M., Nielsen, E. J., and Fisher, T. C., “Towards an entropy stable spectral element framework for computational fluid dynamics,” *54th AIAA Aerospace Sciences Meeting*, 2016, p. 1058.
- [23] Fernández, D. C. D. R., Carpenter, M. H., Dalcin, L., Zampini, S., and Parsani, M., “Entropy stable h/p-nonconforming discretization with the summation-by-parts property for the compressible Euler and Navier–Stokes equations,” *SN Partial Differential Equations and Applications*, Vol. 1, No. 2, 2020, pp. 9.
- [24] Ismail, F. and Roe, P. L., “Affordable, entropy-consistent Euler flux functions II: Entropy production at shocks,” *Journal of Computational Physics*, Vol. 228, No. 15, 2009, pp. 5410–5436.

- [25] Munz, C.-D., Omnes, P., Schneider, R., Sonnendrücker, E., and Voß, U., “Divergence Correction Techniques for Maxwell Solvers Based on a Hyperbolic Model,” *Journal of Computational Physics*, Vol. 161, No. 2, 2000, pp. 484–511.
- [26] Dedner, A., Kemm, F., Kröner, D., Munz, C.-D., Schnitzer, T., and Wesenberg, M., “Hyperbolic Divergence Cleaning for the MHD Equations,” *Journal of Computational Physics*, Vol. 175, No. 2, 2002, pp. 645–673.
- [27] Tricco, T. S., Price, D. J., and Bate, M. R., “Constrained hyperbolic divergence cleaning in smoothed particle magnetohydrodynamics with variable cleaning speeds,” *Journal of Computational Physics*, Vol. 322, 2016, pp. 326–344.
- [28] Svärd, M., “Weak solutions and convergent numerical schemes of modified compressible Navier–Stokes equations,” *Journal of Computational Physics*, Vol. 288, 2015, pp. 19–51.
- [29] Bejan, A., *Entropy Generation Minimization: The Method of Thermodynamic Optimization of Finite-Size Systems and Finite-Time Processes*, Mechanical and Aerospace Engineering Series, Taylor & Francis, 1995.
- [30] Goedbloed, J. P. and Poedts, S., *Principles of magnetohydrodynamics: with applications to laboratory and astrophysical plasmas*, Cambridge university press, 2004.
- [31] Friedrich, L., Winters, A. R., Del Rey Fernández, D. C., Gassner, G. J., Parsani, M., and Carpenter, M. H., “An entropy stable h/p non-conforming discontinuous Galerkin method with the summation-by-parts property,” *Journal of Scientific Computing*, Vol. 77, 2018, pp. 689–725.
- [32] Carpenter, M. H., Parsani, M., Fisher, T. C., and Nielsen, E. J., “Entropy stable staggered grid spectral collocation for the Burgers’ and compressible Navier–Stokes equations,” *NASA/TM-2015-218990*, 2015.
- [33] Carpenter, M. H., Gottlieb, D., and Abarbanel, S., “Time-stable boundary conditions for finite-difference schemes solving hyperbolic systems: Methodology and application to high-order compact schemes,” *Journal of Computational Physics*, Vol. 111, No. 2, 1994, pp. 220–236.
- [34] Carpenter, M. H., Nordström, J., and Gottlieb, D., “A stable and conservative interface treatment of arbitrary spatial accuracy,” *Journal of Computational Physics*, Vol. 148, No. 2, 1999, pp. 341–365.
- [35] Parsani, M., Carpenter, M. H., and Nielsen, E. J., “Entropy stable discontinuous interfaces coupling for the three-dimensional compressible Navier–Stokes equations,” *Journal of Computational Physics*, Vol. 290, 2015, pp. 132–138.
- [36] Parsani, M., Boukharfane, R., Nolasco, I. R., Fernández, D. C. D. R., Zampini, S., Hadri, B., and Dalcin, L., “High-order accurate entropy-stable discontinuous collocated Galerkin methods with the summation-by-parts property for compressible CFD frameworks: Scalable SSDC algorithms and flow solver,” *Journal of Computational Physics*, Vol. 424, 2021, pp. 109844.
- [37] Bassi, F. and Rebay, S., “A high-order accurate discontinuous finite element method for the numerical solution of the compressible Navier–Stokes equations,” *Journal of computational physics*, Vol. 131, No. 2, 1997, pp. 267–279.
- [38] Derigs, D., Winters, A. R., Gassner, G. J., and Walch, S., “A novel averaging technique for discrete entropy-stable dissipation operators for ideal MHD,” *Journal of Computational Physics*, Vol. 330, 2017, pp. 624–632.
- [39] Svärd, M., “A new Eulerian model for viscous and heat conducting compressible flows,” *Physica A: Statistical Mechanics and its Applications*, Vol. 506, 2018, pp. 350–375.
- [40] Sayyari, M., Dalcin, L., and Parsani, M., “Entropy stable no-slip wall boundary conditions for the Eulerian model for viscous and heat conducting compressible flows,” *AIAA Scitech 2021 Forum*, 2021, p. 1662.
- [41] Parsani, M., Boukharfane, R., Nolasco, I. R., Del Rey Fernández, D. C., Zampini, S., Hadri, B., and Dalcin, L., “High-order accurate entropy-stable discontinuous collocated Galerkin methods with the summation-by-parts property for compressible CFD frameworks: Scalable SSDC algorithms and flow solver,” *Journal of Computational Physics*, 2020, pp. 109844.
- [42] Balay, S., Abhyankar, S., Adams, M. F., Benson, S., Brown, J., Brune, P., Buschelman, K., Constantinescu, E., Dalcin, L., Dener, A., Eijkhout, V., Faibussowitsch, J., Gropp, W. D., Hapla, V., Isaac, T., Jolivet, P., Karpeev, D., Kaushik, D., Knepley, M. G., Kong, F., Kruger, S., May, D. A., McInnes, L. C., Mills, R. T., Mitchell, L., Munson, T., Roman, J. E., Rupp, K., Sanan, P., Sarich, J., Smith, B. F., Zampini, S., Zhang, H., Zhang, H., and Zhang, J., “PETSc/TAO Users Manual,” Tech. Rep. ANL-21/39 - Revision 3.21, Argonne National Laboratory, 2024.
- [43] Knepley, M. G. and Karpeev, D. A., “Mesh algorithms for PDE with Sieve I: Mesh distribution,” *Scientific Programming*, Vol. 17, No. 3, 2009, pp. 215–230.
- [44] Abhyankar, S., Brown, J., Constantinescu, E. M., Ghosh, D., Smith, B. F., and Zhang, H., “PETSc/TS: A modern scalable ODE/DAE solver library,” *arXiv preprint [arXiv:1806.01437](https://arxiv.org/abs/1806.01437)*, 2018.
- [45] Fernandez, D. D. R., Carpenter, M. H., Dalcin, L., Friedrich, L., Rojas, D., Winters, A., Gassner, G., Zampini, S., and Parsani, M., “Entropy Stable Nonconforming Discretizations with the Summation-By-Parts Property

- for Curvilinear Coordinates,” *NASA/TM-2020-220574*, 2020.
- [46] Ranocha, H., Sayyari, M., Dalcin, L., Parsani, M., and Ketcheson, D. I., “Relaxation Runge–Kutta Methods: Fully-Discrete Explicit Entropy-Stable Schemes for the Euler and Navier–Stokes Equations,” *Accepted in SIAM Journal on Scientific Computing*, Vol. 42, No. 2, 2019, pp. A612–A638.
 - [47] Al Jahdali, R., Dalcin, L., and Parsani, M., “On the performance of relaxation and adaptive explicit Runge–Kutta schemes for high-order compressible flow simulations,” *Journal of Computational Physics*, Vol. 464, 2022, pp. 111333.
 - [48] Ranocha, H., Dalcin, L., Parsani, M., and Ketcheson, D. I., “Optimized Runge–Kutta Methods with Automatic Step Size Control for Compressible Computational Fluid Dynamics,” *Communications on Applied Mathematics and Computation*, 2021.
 - [49] Fisher, T. C., *High-order L2 stable multi-domain finite difference method for compressible flows*, Ph.D. thesis, Purdue University, 2012.
 - [50] Nolasco, I. R., Dalcin, L., Fernández, D. C. D. R., Zampini, S., and Parsani, M., “Optimized geometrical metrics satisfying free-stream preservation,” *Computers & Fluids*, Vol. 207, 2020, pp. 104555.
 - [51] Geuzaine, C. and Remacle, J.-F., “Gmsh: A 3-D finite element mesh generator with built-in pre-and post-processing facilities,” *International journal for numerical methods in engineering*, Vol. 79, No. 11, 2009, pp. 1309–1331.
 - [52] Hunter, J. D., “Matplotlib: A 2D graphics environment,” *Computing in Science & Engineering*, Vol. 9, No. 3, 2007, pp. 90–95.
 - [53] Ahrens, J., Geveci, B., and Law, C., “ParaView: An End-User Tool for Large-Data Visualization,” *Visualization Handbook*, edited by C. D. Hansen and C. R. Johnson, Butterworth-Heinemann, Burlington, 2005, pp. 717–731.
 - [54] LeVeque, R. J. and LeVeque, R. J., *Numerical methods for conservation laws*, Vol. 214, Springer, 1992.
 - [55] Dormand, J. and Prince, P., “A family of embedded Runge–Kutta formulae,” *Journal of Computational and Applied Mathematics*, Vol. 6, No. 1, 1980, pp. 19–26.
 - [56] Söderlind, G., “Digital filters in adaptive time-stepping,” *ACM Transactions on Mathematical Software (TOMS)*, Vol. 29, No. 1, 2003, pp. 1–26.
 - [57] Söderlind, G. and Wang, L., “Adaptive time-stepping and computational stability,” *Journal of Computational and Applied Mathematics*, Vol. 185, No. 2, 2006, pp. 225–243, Special Issue: International Workshop on the Technological Aspects of Mathematics.
 - [58] Ranocha, H., Winters, A. R., Castro, H. G., Dalcin, L., Schlottke-Lakemper, M., Gassner, G. J., and Parsani, M., “On error-based step size control for discontinuous Galerkin methods for compressible fluid dynamics,” *Communications on Applied Mathematics and Computation*, 2023, pp. 1–37.
 - [59] Ihara, S., Tajima, K., and Matsushima, A., “The flow of conducting fluids in circular pipes with finite conductivity under uniform transverse magnetic fields,” *Journal of Applied Mechanics*, Vol. 34, No. 1, 1967, pp. 29–36.
 - [60] La, M., Kim, W., Yang, W., Kim, H. W., and Kim, D. S., “Design and numerical simulation of complex flow generation in a microchannel by magnetohydrodynamic (MHD) actuation,” *International journal of precision engineering and manufacturing*, Vol. 15, 2014, pp. 463–470.
 - [61] NT-MDT Spectrum Instruments, “Magnetic field of rectangular conductor with current,” [https://web.archive.org/web/20240421215456/https://www.ntmdt-si.com/resources/spm-theory/theoretical-background-of-spm/2-scanning-force-microscopy-\(sfm\)/27-magnetic-force-microscopy-quantitative-results-treatment/279-magnetic-field-of-rectangular-conductor-wi](https://web.archive.org/web/20240421215456/https://www.ntmdt-si.com/resources/spm-theory/theoretical-background-of-spm/2-scanning-force-microscopy-(sfm)/27-magnetic-force-microscopy-quantitative-results-treatment/279-magnetic-field-of-rectangular-conductor-wi) Accessed: 21-Apr-2024.
 - [62] Dennison, E., “Off-axis Magnetic Field of a Circular Current Loop,” http://web.archive.org/web/20240430063620/https://tigerntatie.github.io/emagnet-py/offaxis/off_axis_loop.html, Accessed: 30-Apr-2024.
 - [63] Jackson, J. D., *Classical Electrodynamics*, Wiley, New York, 3rd ed., 1999.
 - [64] Burton, R., Clark, K., and Jahn, R., “Measured performance of a multimegawatt MPD thruster,” *Journal of Spacecraft and Rockets*, Vol. 20, No. 3, 1983, pp. 299–304.
 - [65] Sankaran, K., Choueiri, E., and Jardin, S., “Comparison of simulated magnetoplasma dynamic thruster flowfields to experimental measurements,” *Journal of propulsion and power*, Vol. 21, No. 1, 2005, pp. 129–138.
 - [66] Mayigüé, C. C. and Groll, R., “Numerical simulation of Argon fuelled self-field magnetoplasma dynamic thrusters using the central-upwind scheme flux interpolations,” *European Journal of Mechanics-B/Fluids*, Vol. 72, 2018, pp. 645–663.